DESIGN, ANALYSIS, AND TESTING OF A METAL MATRIX COMPOSITE WEB/FLANGE INTERSECTION

S. B. Biggers and N. F. Knight, Jr.
Department of Mechanical Engineering
Clemson University, Clemson, SC

S.G. Moran*
NASA Headquarters
Washington, D.C.

R. Olliffe
Lockheed Aeronautical Systems Company
Marietta, GA

*Formerly employed by
Lockheed Aeronautical Systems Company

SUMMARY

An experimental and analytical program to investigate the local design details of a typical T–shaped web/flange intersection made from a metal matrix composite is described. Loads creating flange bending were applied to specimens having different designs and boundary conditions. Finite element analyses were conducted on models of the test specimens to predict the structural response. The analyses correctly predict failure load, mode, and location in the fillet material in the intersection region of the web and the flange when specimen quality is good. The test program shows the importance of fabrication quality in the intersection region. The full–scale test program that led to the investigation of this local detail is also described.

INTRODUCTION

Full–scale tests conducted at Lockheed Aeronautical Systems Company (LASC) under Air Force Wright Laboratory (AFWL) sponsorship revealed an unexpected failure mode for continuous–fiber–reinforced (CFR) metal matrix composites (MMC). During fatigue testing of a full–scale vertical tail structure, the front and rear spars cracked along their fillet radius, with the beam cap flanges separating from the webs. The spars are I–section beams made of silicon carbide CFR 6061 aluminum (SiCf/Al). Failures of this type had not occurred in any of the previous structural element or subcomponent tests conducted to uncover potential problems prior to full–scale testing. Fillet shear strength and cyclic three–point bending tests conducted on intact remnants of the failed spars indicated that shear transfer from web to flange was not the cause of failure. It was, therefore, concluded that out–of–plane loading creating local bending of the spar flanges was the probable cause. This conclusion is supported by the fact that one of the failures in the full–scale test appeared to originate near a load introduction fitting. In addition, some mismatch was observed between the skin, spar, and intercostal that resulted in local bending of the flange during assembly.

Recognizing that local out-of-plane loading on the flanges is likely to occur due to a number of unavoidable sources, a study was initiated in an LASC Independent Research and Development (IRAD) program to determine the causes and possible solutions for failures in the web/flange intersection region. A test program was defined to evaluate variations in the local design detail of the web/flange intersection region. Test specimens were fabricated with eight different fillet configurations using SiCf/Al. Finite element analyses of the web/flange intersection region were conducted to evaluate the effect of the fillet configuration on the stress state. The analysis also helped to define testing conditions which would best expose the out-of-plane weakness of the specimens, thereby fully testing the ability of the fillet design variations to delay or prevent out-of-plane failures.

This paper summarizes the full-scale testing in which the problem first appeared, the development testing leading up to the full-scale test program, and the test results for the web/flange intersection specimen testing. It describes the web/flange intersection finite element model development, the analysis results obtained, and correlation of the test and analysis results.

DESIGN DEVELOPMENT AND FULL-SCALE TESTING

Since 1981, the AFWL's Advanced Metallic Structures Program Office has funded LASC to design, fabricate, and test four metal matrix composite (MMC) vertical tails representative of advanced fighter structure. One of the partially assembled vertical tail structures is shown in Figure 1 prior to installation of the near side outer skin panels. The process leading to fabrication of the full-scale test articles included extensive material characterization testing at the coupon level to develop statistically significant design allowables to support detail design and analysis; element testing of joints, stiffened panels, and large subcomponents to verify MMC analysis methods; and design verification element testing to investigate critical vertical tail design details such as the root fitting, the skin/rib/spar intersection, and hinge fitting attachment.

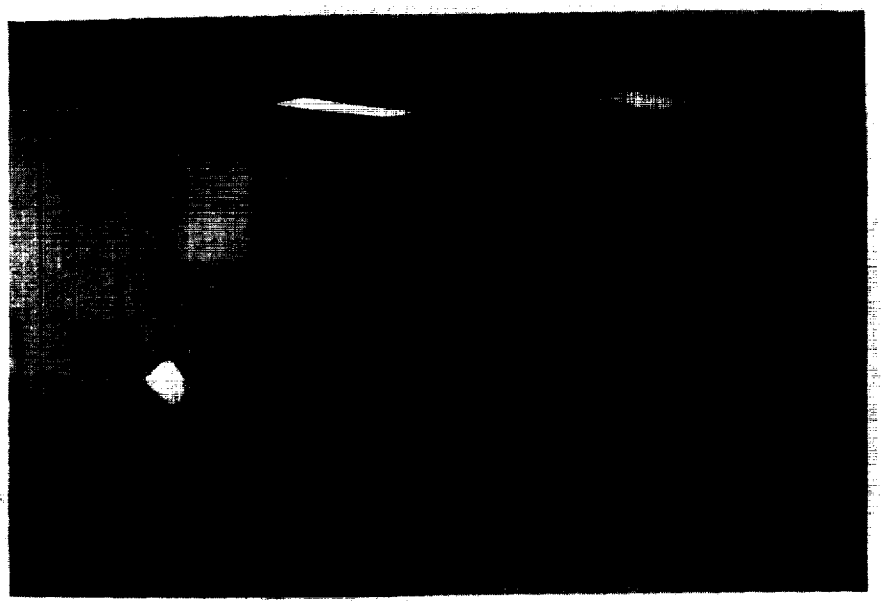

Figure 1. Partially Assembled MMC Vertical Tail Structure.

Two different multi–spar vertical tail configurations were designed, one with discontinuous silicon carbide whisker reinforced aluminum (SiCw/Al) skins (referred to in this paper as the SiCw/Al test article) and the other with continuous silicon carbide fiber reinforced aluminum (SiCf/Al) skins (referred to as the SiCf/Al test article). Both designs had the same substructure, consisting of five hot–molded SiCf/Al spars approximately ten feet long (fabricated by Textron Specialty Materials Division) joined by fourteen hot formed SiCw/Al intercostals (fabricated from large sheet supplied by Advanced Composite Materials Corporation). One static and one fatigue test article was fabricated for each configuration, for a total of four full–scale test articles.

SiCf/Al Spar Hot Molding Process Development

As shown in Figure 2, each SiCf/Al spar consists of nine individual components — two preconsolidated flange plates, a preconsolidated centerline web element, two preconsolidated channel sections which serve to tie the flanges to the webs, and four fillet radius fillers. In addition, a small gap exists between the web and flange that becomes filled with the filler material used in the fillets upon hot molding. The basic design configuration and tooling concept for these SiCf/Al spars were developed and evaluated in the SiCf/Al hot molding process development program conducted by Textron Specialty Materials Division during the initial stages of the AFWL contract.

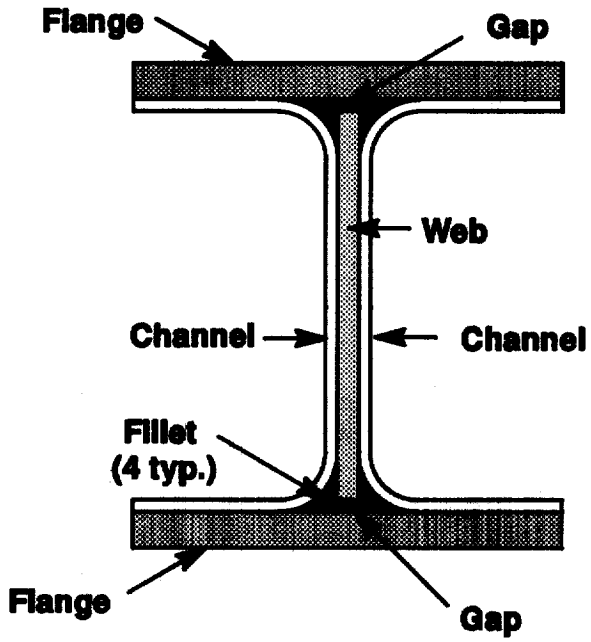

Figure 2. Individual components of a SiCf/Al spar.

The original intent in designing the SiCf/Al spars was to include 90–degree plies in the channel sections to improve pull–off strength. However, early development tests of the 5.6 mil diameter SiC fiber indicated that the minimum radius for 90–degree plies was too large to allow fabrication of practical structural shapes. The 90–degree plies were subsequently eliminated, and the spar fillet radius was dictated by the minimum radius (.25 in.) for wrapping 45–degree plies.

It was assumed in the early stages of design development that the web/flange intersection in hot molded SiCf/Al shapes would develop approximately the same shear carrying capability as unidirectional panels, i.e., 15 ksi. However, tests conducted as part of the hot molding process development efforts revealed that, even with 45–degree plies in the channel sections, the required flange pull–off strength and web/flange shear strength were not achieved due to incomplete consolidation in the fillet area of the web/flange intersection region. Through improvements in both the matrix materials and the hot molding process parameters, the fillet shear strength was improved to within acceptable limits, but never achieved a strength equivalent to that of unidirectional panels.

SiCf/Al Spar Qualification Tests

Based on lessons learned in the hot molding process development program, a qualification test was designed to measure the fillet shear strength of every SiCf/Al spar used in the full–scale test article fabrication. Samples were removed from the root and tip of each incoming spar and subjected to a special LASC–developed shear strength test. The results of these tests are shown in Figure 3 as high and low values from four tests for the root and tip segments of each spar. Also shown are finite element analysis predictions of the maximum shear loads for each spar. These maximum values usually occurred near the root.

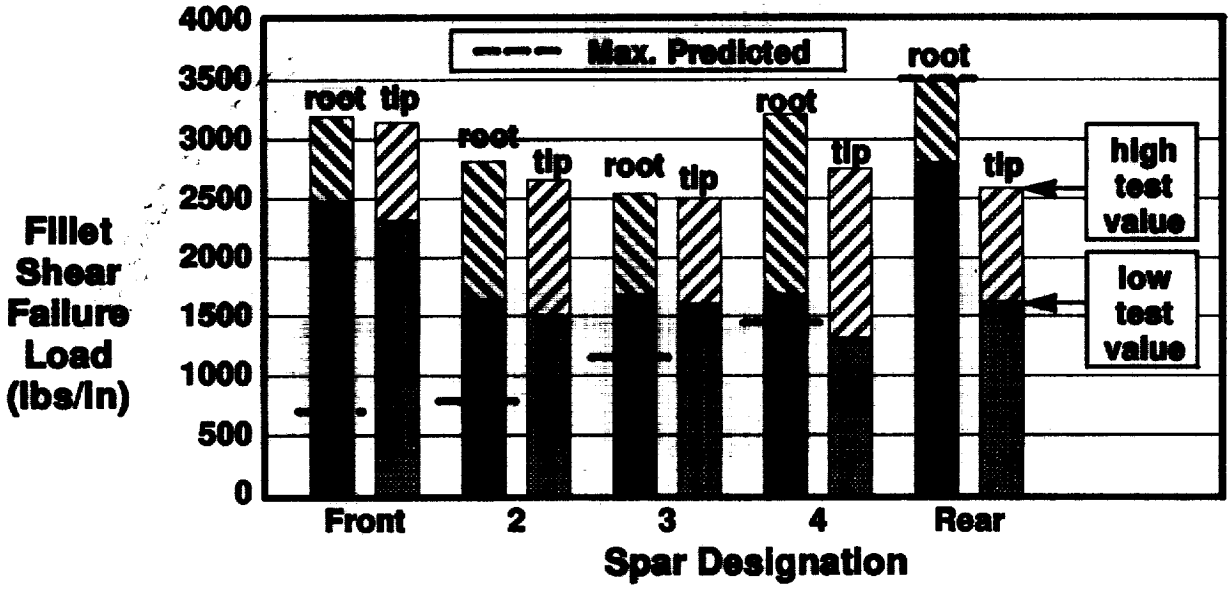

Figure 3. Measured and predicted fillet shear strength in each spar.

Although the range between the high and low strength values is significant, indicating a wide variation in fillet shear strength from spar to spar and possibly within individual spars, all of the strengths were above the predicted strength requirement except for the rear spar (minimum of 2807 lbs/in. at the root versus 3524 lbs/in. required). Based on the spar qualification test results, the full– scale test article designs were modified by bonding titanium doublers in the fillet radii of the rear spars near the root.

Design Development Element and Subcomponent Tests

Element and subcomponent tests conducted in support of preliminary design of the vertical tail structure included static and fatigue tests of chordwise joints, spanwise splices, and skin/stiffener tension and compression panels; multiple-stiffener buckling resistant and post-buckled compression and shear panels; pressure box tests of a stiffened skin panel; and a combined shear-compression-pressure test of a large stiffened fuselage shell subcomponent. In addition, several element tests were conducted to verify vertical tail design details. These verification elements included a static test of the rudder hinge fitting and fatigue tests of the skin/rib/spar intersection and the intersection of the skin and spar with the titanium root fitting. The results of these tests indicated that the analysis methods being used were quite accurate in predicting both buckling and failure loads. Although some minor damage to the SiCf/Al spars occurred during assembly of the elements and subcomponents, none of the static or fatigue tests revealed a problem with the web/flange fillet. All testing conducted prior to the full-scale vertical tail tests indicated that, although the fillet might be a weak link, its strength was adequate for the intended design once the fillet consolidation problem was solved. The spar qualification tests also supported this conclusion.

Full-Scale Test Setup

The full-scale vertical tail structural tests were conducted in a specially constructed loading frame. Five hydraulic jacks applied loads at discrete points along the front and rear spars and two jacks were used to load the tip of the tail through a loading "cradle." The discrete load points included three on the front spar at the spar/rib intersections and two on the rear spar at the upper and lower rudder hinge fittings. In the photographs shown in Figure 4, the front spar is at the top of the test article, and the rear spar hinge fitting load points can be seen at the bottom of the article. Loads were reacted through a titanium root fitting attached to the steel load frame, simulating the fuselage attachment. All loading jacks were capable of reversed loading, so that all bending and torsion load cases could be applied. The test articles were instrumented with over 220 strain gages, thermocouples, and displacement transducers.

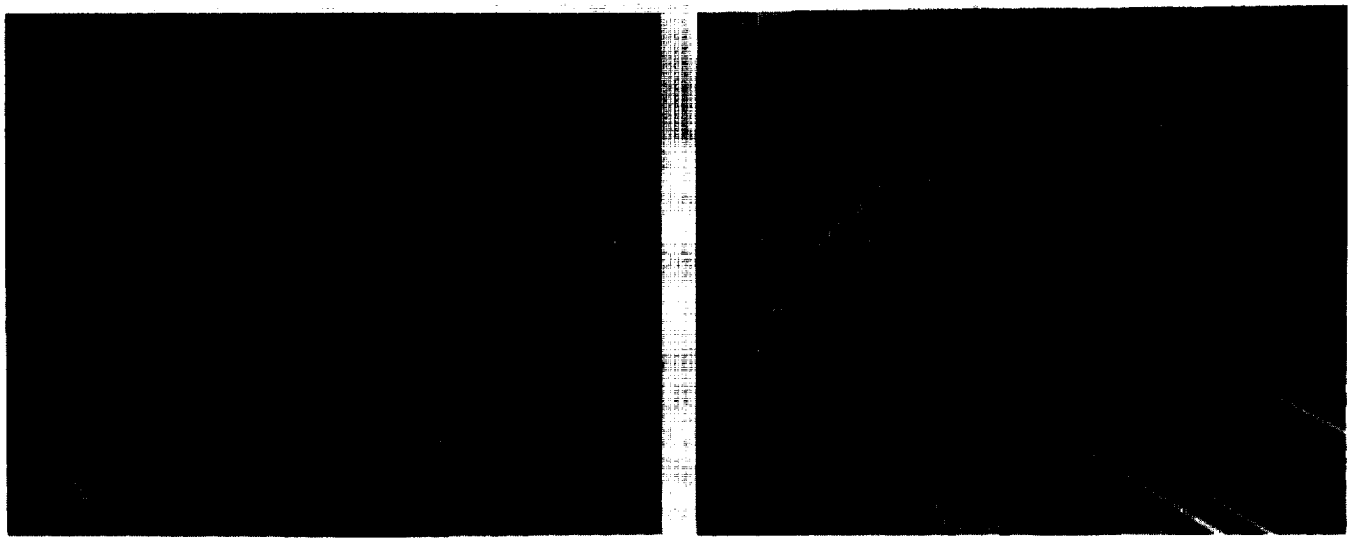

Figure 4. Full-scale structural test setup.

Full-Scale Static Tests

The first full-scale structural test was conducted on the SiCw/Al static test article. This test was conducted at temperature in a specially designed environmental chamber to simulate the actual flight environment (250°F). During design limit load (DLL) application at temperature, buckling of the two-sheet bonded SiCw/Al skins occurred well before the analytically predicted load levels were reached. Analysis of the strain gage data indicated that the adhesive bond in the two-sheet bonded skin softened enough at the elevated temperature to allow the two skin sheets to buckle independently. As a result, the subsequent ultimate load condition was applied at room temperature. Failure occurred at approximately 142% of DLL. It was difficult to determine the exact failure sequence, but post-test investigations indicated that the failure originated in Spar No. 3 (the center spar) by either flange buckling due to lack of support from the postbuckled skin or by flange bending caused by the out-of-plane loads applied by the postbuckled skin. The failure resulted in total separation of the spar flange from the web along the web/flange fillet.

Since there was no adhesive bond in the skin of the SiCf/Al test article, the full-scale SiCf/Al ultimate load test was conducted in the environmental chamber at 250°F. The limit load applications at room and elevated temperatures were accomplished without problem. Correlation of analytically predicted (finite element method) and measured strains at limit load are shown in Figure 5.

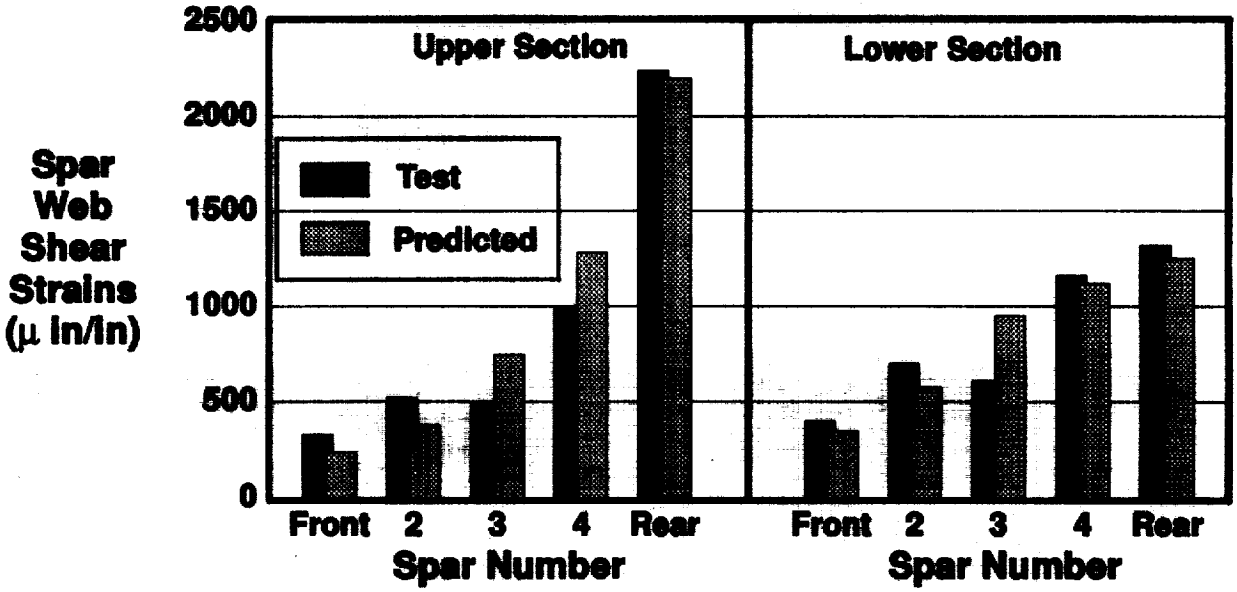

Figure 5. Predicted and measured spar web strains at limit load.

However, during application of ultimate load (150% of DLL), the load control system released all load at approximately 140% of DLL. Visual inspection from outside the environmental chamber revealed no apparent damage, so the control system was reset and load was applied again. The control system again released all load at approximately 120% of DLL, again with no apparent visible damage. The control system was reset and, on the third attempt to apply ultimate load, the test article failed at 50% of DLL. Post-test failure investigations indicated that the initial failure probably occurred at 140% of DLL by separation of the rear spar flange from the web at the flange/web fillet near the upper hinge fitting. Upon subsequent applications of load,

the flange separation progressed to the point that the spar could no longer support the skin. This change in local boundary conditions and major load redistribution caused the skin to buckle and led to total failure of the test article.

Full-Scale Fatigue Tests

The fatigue test plan of the full-scale cyclic test articles included two lifetimes of durability testing followed by one lifetime of damage tolerance testing. Each lifetime was composed of approximately 166,000 cycles of truncated spectrum loading representing the primary damaging cycles of the fatigue spectrum. These cycles were contained in 32 repeatable "passes," each composed of 124 unique "flights," for a total of 3968 "flights" per lifetime. Due to the difficulties encountered in the elevated temperature static tests, the fatigue tests were conducted at room temperature.

The SiCw/Al cyclic test article was accidentally damaged during test system checkout. A large undamaged subcomponent was subsequently tested under LASC IRAD. Problems were also encountered during fatigue testing of the SiCf/Al cyclic test article. Testing was interrupted after 308 flights, or approximately 8% of the first lifetime of durability testing, due to failure of the front spar web/flange fillet. Figure 6 shows a close up view of the failure along the compression flange of the front spar.

Figure 6. View of web/flange intersection fatigue failure in front spar.

Post-Test Failure Investigation

To determine whether the front spar fillets had adequate static shear strength, three fillet shear strength tests similar to the spar qualification tests were conducted on undamaged specimens removed from the upper, middle and lower sections of the failed spar. Fillet shear strengths measured 1930, 2490, and 2595 lbs/in., respectively, in the three tests. Although there was a wide variation in the strength of the front spar fillets, their strength was well above the required shear strength of 719 lbs/in.

Prior to the failure of the front spar, no cyclic tests had been conducted which included load transfer between the flange and web through bending. To determine whether cyclic shear

was causing the fatigue cracking of the spar fillets, two 3–point bending fatigue tests were conducted on undamaged segments removed from previously tested full–scale articles. Instrumentation of the test specimens included spar flange axial gages and spar web shear gages. The test setup is shown in Figure 7.

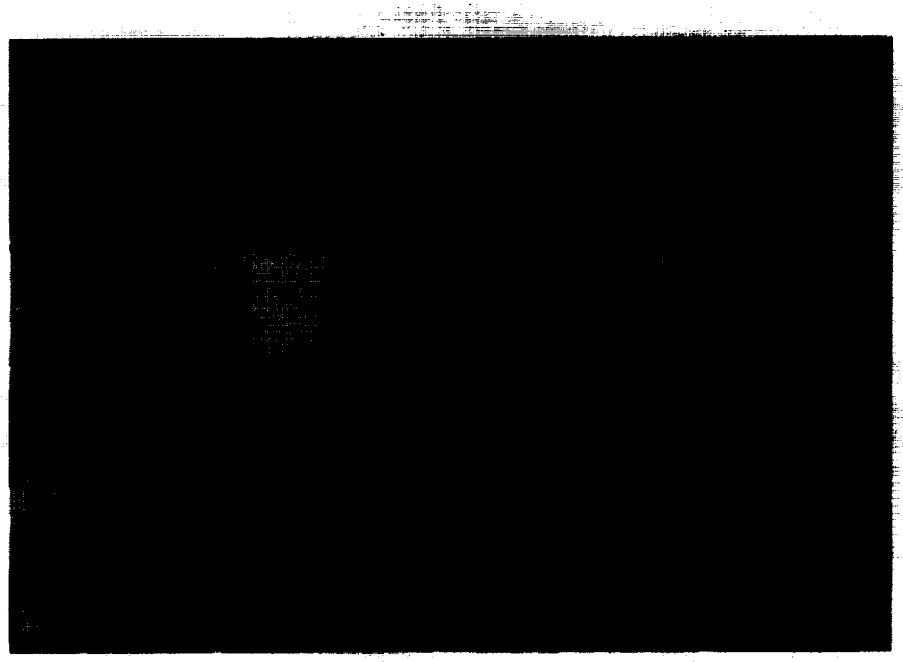

Figure 7. Three–point bending test setup.

The loads were adjusted to obtain spar flange axial and web shear strains which closely matched the strains measured during full–scale test of one of the critical load cases. For the front spar, these strains were 525 μ–in/in. in the flange and 617 μ–in/in. in the web; for the rear spar, they were 1000 μ–in/in. in the flange and 1600 μ–in/in. in the web. The specimens were cycled at constant amplitude with a minimum to maximum load ratio R = 0.1.

The test specimen representing the upper section of the front spar achieved 74,600 cycles at maximum strain (considerably more than the full–scale test article would experience in three lifetimes of fatigue testing) before the test was stopped. A 0.25 inch saw cut simulating a web/flange crack was then placed in the compression fillet midway between the load and reaction points and the specimen was subjected to an additional 14,000 cycles at maximum strain with no failure and no apparent crack growth. The loads were increased 50% and the specimen was cycled an additional 60,000 cycles with no failure or apparent crack growth. At this point the test was discontinued.

The test specimen representing the root of the rear spar achieved 42,500 cycles at maximum strain (again, considerably more than would be seen by the full–scale article in three lifetimes of testing) with no apparent degradation. The loads were increased 25% and the specimen was subjected to an additional 2000 cycles with no damage. A saw cut was inserted in the compression fillet and the specimen was cycled an additional 11,000 cycles at the increased load level with no failure and no apparent crack growth, at which time the test was discontinued.

The results of the static fillet shear strength tests and the 3–point bending fatigue tests indicated that the spar fillets had more than adequate static and fatigue shear strength to sustain the analytically predicted loads for the three lifetimes of fatigue testing. Based on these results, it was concluded that the spar failed due to unpredicted out–of–plane loads on the flange creating local bending in the web/flange intersection region. These loads may have been caused during assembly by pulling down gaps between the SiCf/Al skins and spar flanges or by local deformations associated with the load introduction fittings. These conclusions were reinforced by the fact that failure of the web/flange intersection did not appear in any of the extensive element, subcomponent, and design verification tests conducted prior to the full–scale tests.

Continued Full–Scale SiCf/Al Fatigue Test

To support a decision to repair and continue fatigue testing of the SiCf/Al cyclic test article, the fillet regions of the spars which had not failed were visually and ultrasonically inspected (using A scan) for additional damage. Since it was not feasible from either a schedule or cost standpoint to fabricate a new SiCf/Al front spar, an equivalent stiffness conventional aluminum spar was designed to replace the failed spar. As safety precautions, crack sensors were placed in all four fillets along the span of the four remaining undamaged spars (a total of 64 crack gages) and the number of visual inspection intervals was substantially increased to detect any possible future cracks before they could lead to further damage. The cyclic test article was reassembled, strain surveys were conducted to ensure that the new aluminum front spar did not significantly affect the strain levels or distributions in the remaining structure, and the fatigue test was resumed.

After an additional 199 flights of fatigue testing, a small crack was detected in one of the rear spar fillets near the lower hinge fitting. Video cameras were set up to record crack growth and the fatigue testing was continued until the crack grew to a significant percentage of the overall span. Testing was discontinued and the LASC IRAD–funded SiCf/Al Fillet Investigation Study reported in the remainder of this paper was initiated to determine the causes for and potential solutions to this problem in the web/flange intersection.

T–SPECIMEN ELEMENT TESTING

To examine the effects of the web/flange intersection design, T–shaped specimens were fabricated using two fillet radii (1/4 in. and 1/2 in.) and different filler materials for the fillet region. A schematic that shows the basic construction of the T–sections is presented in Figure 8. Filler materials with four fiber–volume–content percentages (0%, 17%, 33%, and 50%) were used for this purpose. It was conjectured that the more compliant low fiber–volume filler material might perform better in helping transfer flange bending stresses across the intersection. Preliminary analytical results predicted that the larger fillet radius configuration would delay failures originating in the intersection region due to high interlaminar stresses.

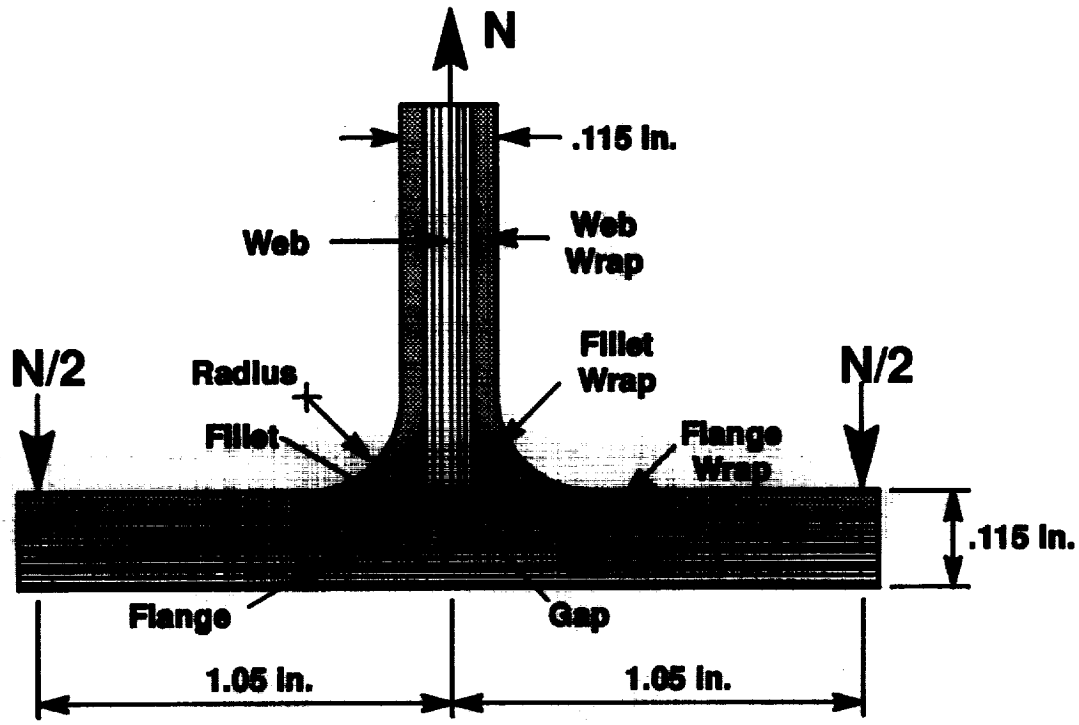

Figure 8. Schematic of T–section test geometry and nomenclature.

The basic fabrication approach is the same as that used in the spars for the full–scale test articles. The bulk of the flange laminate is formed by a preconsolidated laminate with continuous, uniform thickness, horizontal plies. A similar preconsolidated laminate comprises the central core of the web. A pair of ± 45 degree plies with continuous fiber orientations wraps around the fillet radius region and completes the flange and web laminates. Filler material is placed in the fillet regions. A variable sized "gap" exists between the preconsolidated web and flange laminates and is filled with the same material that is in the fillet radius region. This gap is on the order of two to eight ply thicknesses (nominal ply thickness is 7 mils). The inner radius of the wrap plies is either 1/4 or 1/2 inch. Including the wrap plies, the web stacking sequence is $[\pm 45/90/ \mp 45/0/ \pm 45]_s$ and, starting from the inside (web side) of the flange, the right flange stacking sequence is $[\pm 45/0/ \pm 45/0_8/ \mp 45/0]$. The corresponding left flange stacking sequence is $[\mp 45/0/ \pm 45/0_8/ \mp 45/0]$. The 0–degree direction referred to here is perpendicular to the plane of the model.

Specimens were cut from a single I–beam which was fabricated from SiCf/Al and incorporated three specimens of eight different design variations. A schematic of the beam and locations from which 48 T–specimens were taken is shown in Figure 9. Of this total, 46 specimens were tested to failure by symmetrically loading the web in tension and the flanges in downward bending as shown in Figure 8. In 23 of the tests the loads were applied to the flanges through rollers to simulate a simply supported condition. In the remaining tests, the flange loads were applied while clamping the flange ends to prevent rotation. Assembly conditions encountered in actual applications would fall somewhere between these two extreme boundary conditions. Each specimen was statically loaded to failure in a 60–kip Tinius Olsen Universal Test Machine used at a 2400 lb. range with an accuracy of ±0.5 percent of the indicated load.

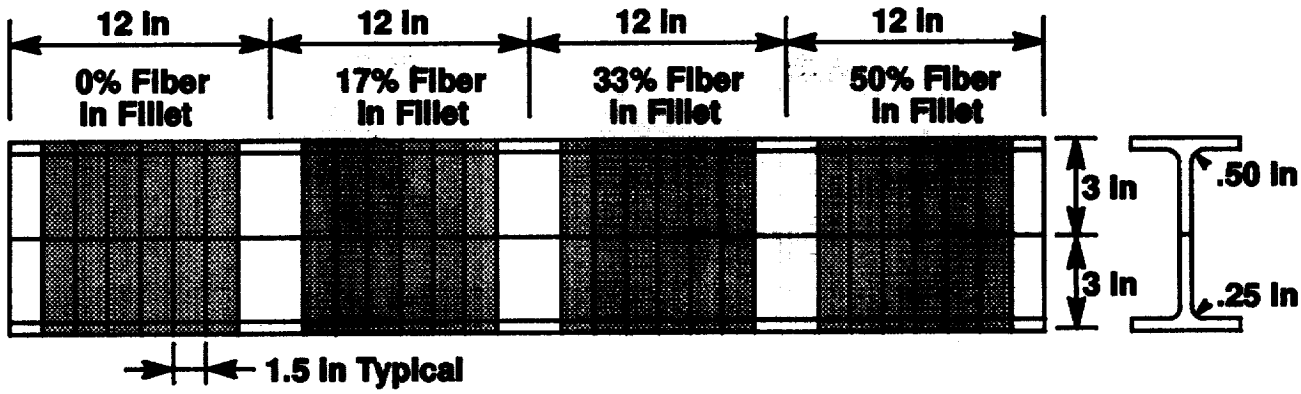

Figure 9. Fabricated I-beam from which T-specimens were taken.

Photographs of typical failed specimens are shown in Figures 10 and 11 for the 1/4-inch radius and the 1/2-inch radius specimens, respectively. In all cases, failure of the specimens initiated due to transverse cracking of the fillet material and/or delamination of the wrap plies from the fillet material. In some cases, delamination within the flange also occurred.

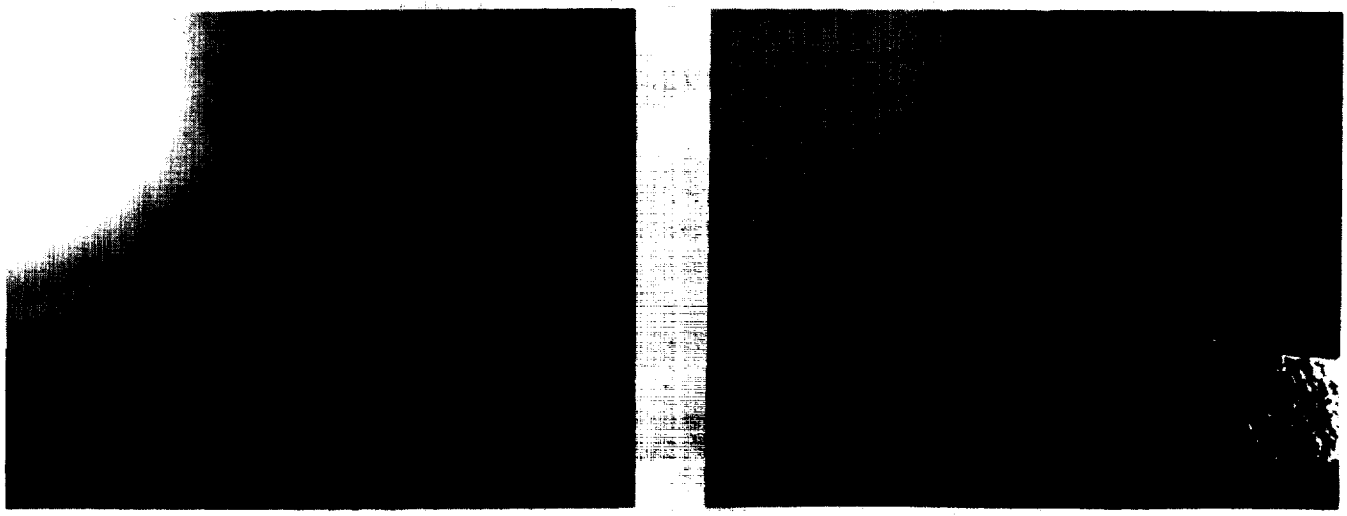

Figure 10. Intersection region of failed 1/4 inch radius specimens.

A summary of all experimentally obtained failure loads is presented in Figures 12 and 13. Consider first the results from the tests on the 1/4 inch radius specimens. Based on the average failure load of the three tests for each configuration, indicated by the dashed lines, there is some evidence that the 50 percent fiber-volume content material in the fillet produces a slightly higher failure load than the other fillet materials in both the simply supported case (Figure 12(a)) and the clamped edge case (Figure 13(a)). In addition, the test results for the 50 percent material are more consistent than with any of the others tested. It should be noted that the 50 percent, 1/4 inch radius configuration was used in the full-scale test article spars.

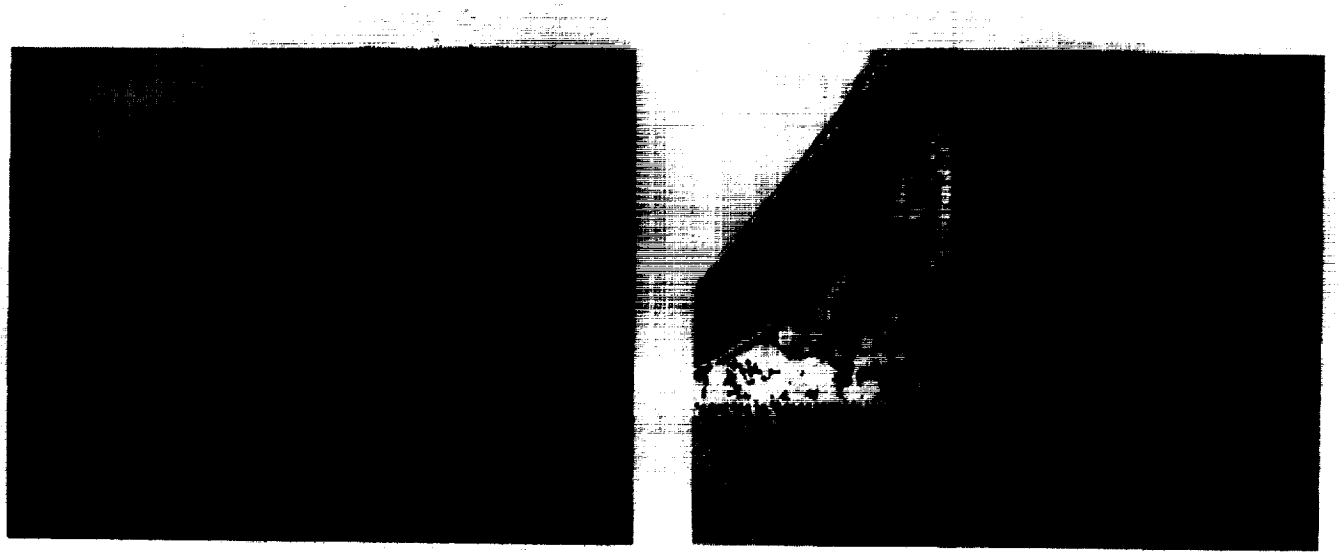

Figure 11. Intersection region of failed 1/2 inch radius specimens.

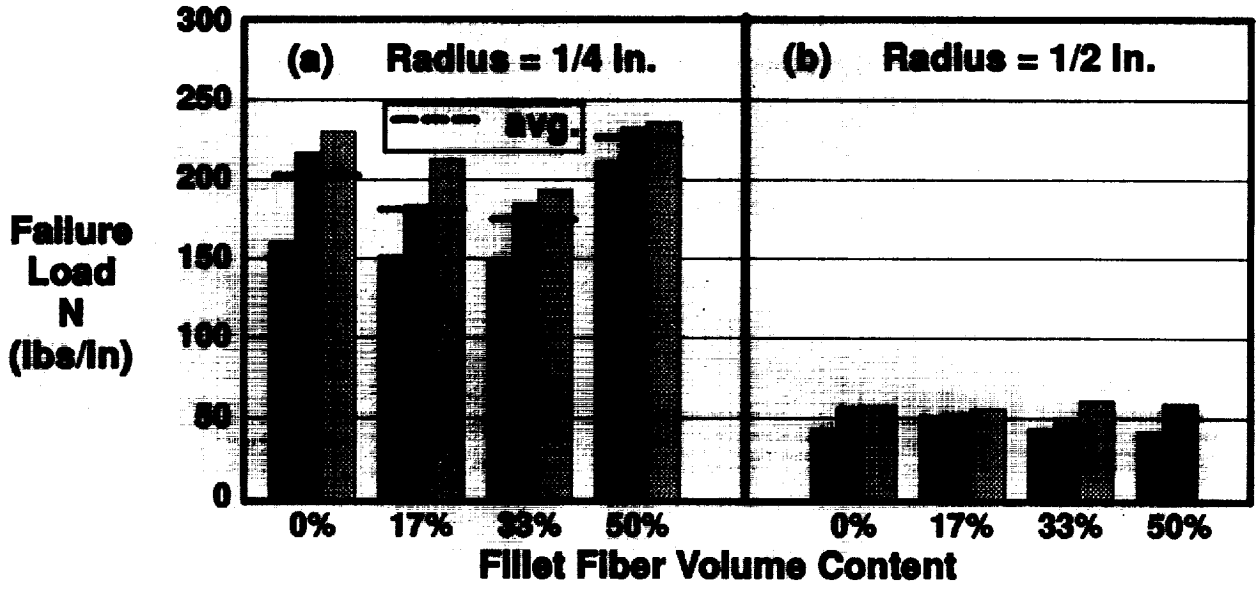

Figure 12. Test results for simply supported specimens.

Contrary to the analytical predictions to be discussed subsequently, the larger radius specimens all failed at much lower loads (see Figures 12(b) and 13(b)) than did the smaller radius specimens. Examination of the specimens prior to testing showed that the material in the critical intersection region of the 1/2 inch radius specimens was not well consolidated, making the results of these tests of questionable validity. This lack of consolidation is indicated in the post-failure photograph in Figure 11, where distinct bundles of MMC wires used to fill the fillet region can be seen. It should be noted that the hot molding process development was carried out for the 1/4 inch radius only.

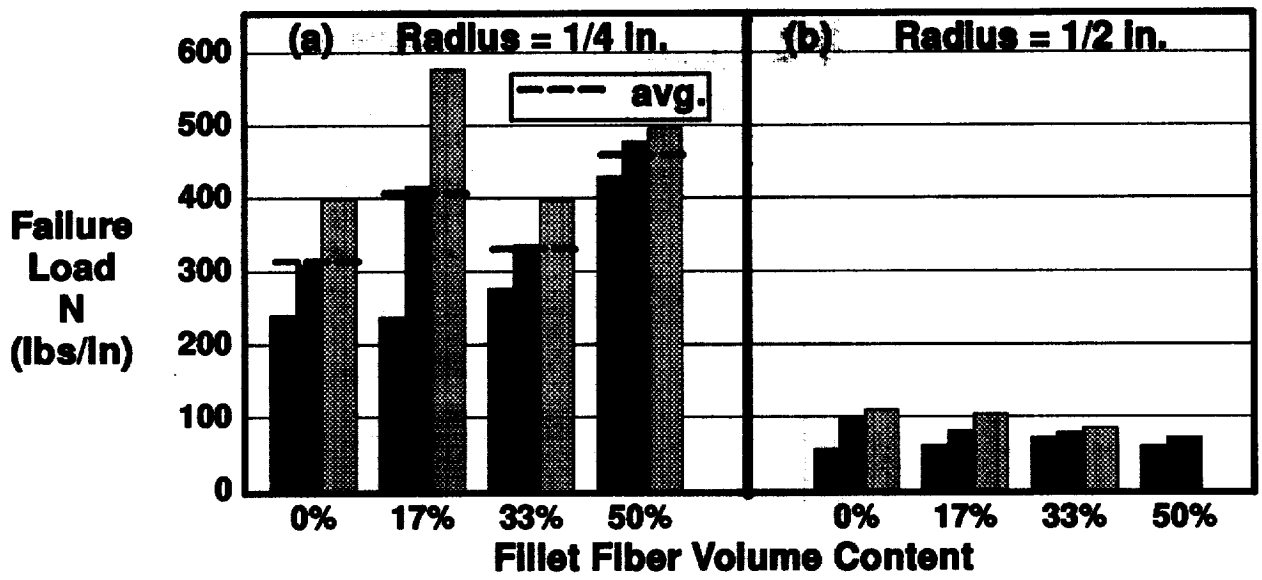

Figure 13. Test results for clamped edge specimens.

Comparison of the average failure loads in Figures 12 and 13 shows that the clamped specimens fail at loads that are 1.6 to 2.2 times higher than the failure loads of the simply supported specimens. This increase is consistent with an elementary beam analysis of the flange which shows a reduction in the maximum bending moment by a factor of 2.0 for the clamped case compared to the simply supported case.

Even though the test results for the 1/2 inch radius specimens are of little quantitative value due to the poor consolidation in the intersection region, they do point out the importance of fabrication quality in this critical region. Since the web and flange sublaminates were identically preconsolidated for the 1/4 inch and the 1/2 inch radius specimens, the low failure loads for the latter provide confirmation that the critical failure arises from the transverse tensile stresses in the 0–degree filler material in the intersection region. In these tests, no effect of fillet material fiber volume percentage is evident, as expected, since all these specimens were approximately equally flawed.

FINITE ELEMENT MODELING OF T-SPECIMENS

The purpose of the analytical investigation was to develop detailed finite element models of the T–section specimens described previously. These models allow the laminar and interlaminar stresses to be evaluated in the region of the web/flange intersection when loads creating local bending are applied. A generic model has been developed with the aim of easy variation of the geometric and material parameters so that the effects of such variations could be evaluated and an improved design developed. Specific models have been used to evaluate the local stress state in a typical test for geometries with two different fillet radii for two types of loading.

A model of a typical cross–sectional slice of the T–section is illustrated in Figure 14. Second–order, isoparametric, generalized plane–strain elements with a capability to represent fully

anisotropic material properties have been used. These elements allow most of the important laminar and interlaminar stresses to be evaluated. The wrapped plies in the critical fillet region are modeled appropriately as curved elements. The generalized plane–strain condition allows stresses perpendicular to the cross–section to be evaluated in conjunction with the laminar and interlaminar stresses in the plane of the model. Each lamina may be modeled through its thickness by one or more elements. The material properties associated with various fiber orientations of each layer in the model may be specified so that any laminate layup and stacking sequence may be considered. The number of plies in each of these laminates may be easily changed.

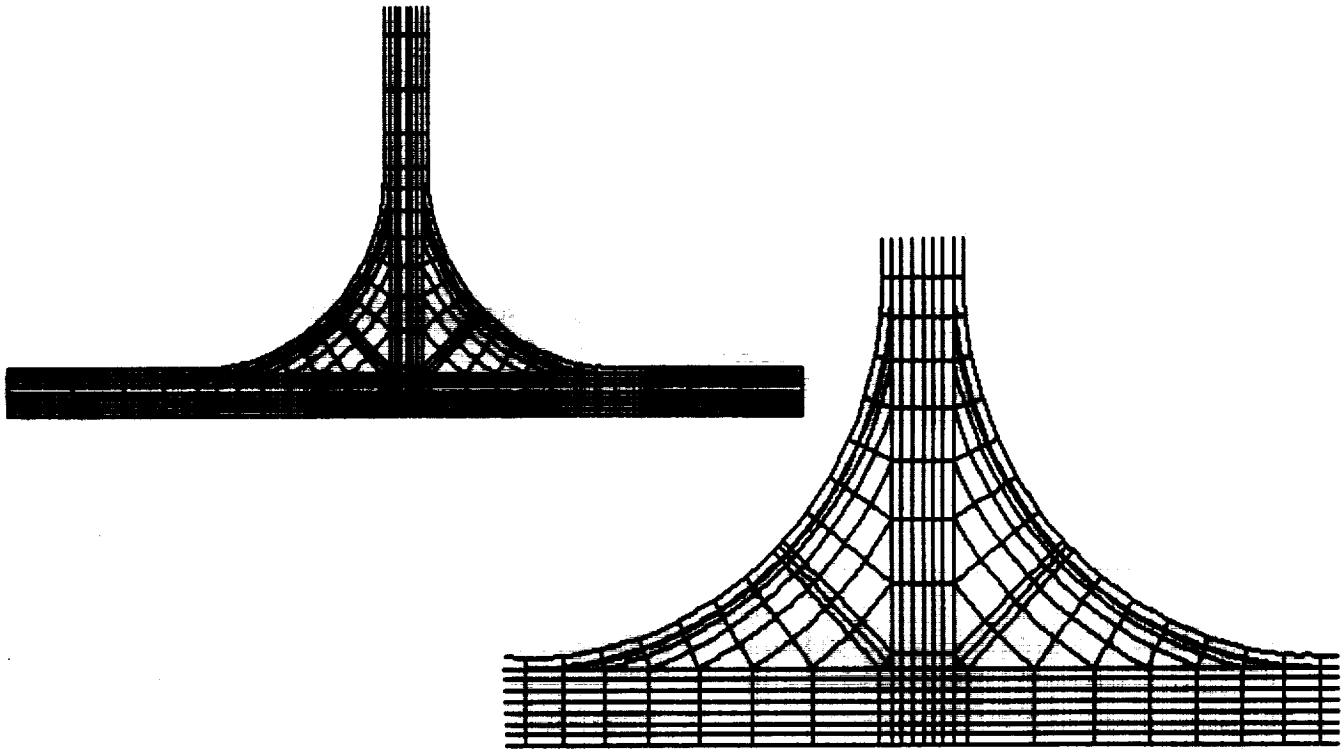

Figure 14. Finite element model mesh pattern for a typical isotropic T–specimen with a 1/2 inch fillet radius and a close–up view of the intersection region.

Boundary conditions may be defined to represent a variety of test configurations. In the results presented herein, the end of the web laminate is assumed to be fixed, and the ends of the left and right flanges are loaded by concentrated normal forces, either symmetrically or antisymmetrically about the web center–line. These conditions allow the stresses associated with flange and web bending to be developed. For these loading conditions, a half–model could be used to evaluate the response of the specimen with reduced computation time if the non–symmetry of the T–section laminates is neglected. This non–symmetry occurs in any T–shaped composite section if unidirectional materials oriented at an angle to the length of the section are used in the wrap plies. A designer may choose either to have both left and right flange laminates symmetric and the web laminate nonsymmetric, or to have the web and one flange symmetric with the remaining flange nonsymmetric. As more plies are used in the wrap and fewer in the web and flange base laminates, these effects should become more important. A full model that accounts for non–symmetry has been used to obtain the results reported herein.

It may be noted from Figure 14 that the lengths of elements in the plies may vary except in the region of the flange directly under the web. This gradation of element lengths allows smaller elements to be defined in the critical regions where the wrap plies become tangent to the web and flange. In addition, very thin and similarly short elements are used in the fillet radius region near the wrap plies. As will be shown in some sample results, these regions develop relatively large stresses both in the laminar directions and in the interlaminar directions. This result bears out the assumption that local flange bending may be a major contributor to the observed failure near the fillet radius region in the box tests and in the T–element tests.

ANALYSIS RESULTS FOR ISOTROPIC MODELS

As initial checks on the model, two models with isotropic properties were created. Analysis of the results for even these simple cases indicates to some extent the important effects of the fillet–radius region geometric parameters on the stresses in this region. For example, consider an aluminum T–section with the dimensions shown in Figure 8. These dimensions are representative of the MMC specimens tested as previously described. Concentrated loads are applied at the ends of the flanges. No restriction of rotation is imposed at the load locations. The distribution and relative magnitudes of the stresses are of primary interest. However, to put a scale on these results, vertical loads of 200 lbs/inch were applied at each flange end in the case of a symmetrically loaded model. With a 1/4 inch fillet radius, the resulting vertical deflection of the tips of the flanges is 0.036 inches and the maximum tensile principal stress found in the model is 78 ksi. The antisymmetric load case was chosen to create the same moment (based on centerline dimensions) on the web as was created on the flanges in the symmetric case. That is, equal and opposite vertical loads of 100 lbs/inch each were applied at the flange ends. The horizontal deflection of the flange is 0.091 inches, the vertical deflection of the tips of the flanges is 0.155 inches, and the maximum tensile principle stress is 104 ksi in this antisymmetric case. Typical deformed shapes, with the deformations magnified for clarity, are shown in Figure 15.

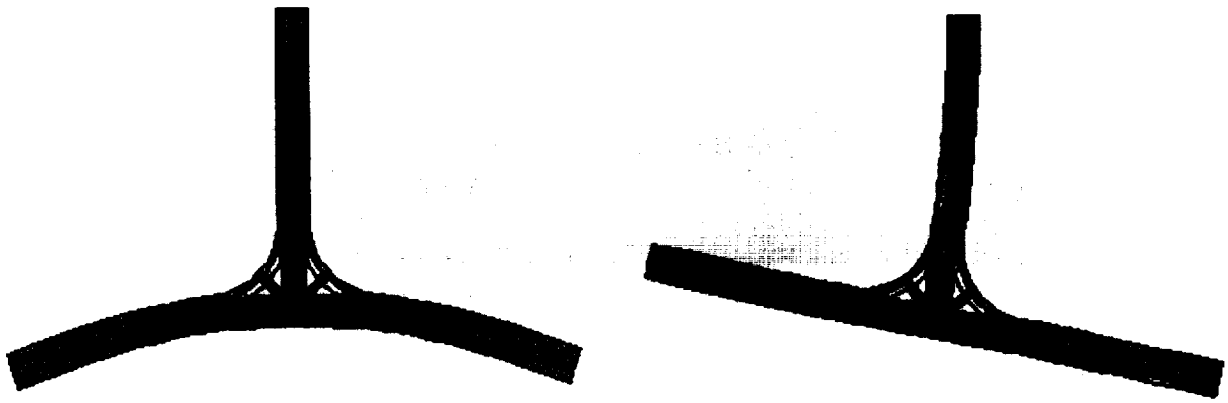

Figure 15. Symmetric and antisymmetric deformations of an isotropic T–specimen.

Symmetric Load Case

Contour plots of the normal stresses in the intersection region are shown in Figures 16 and 17 for the global horizontal direction (σ_{xx}) and the vertical direction (σ_{yy}), respectively. It should be noted that since the stresses shown are all in the global direction, they must be combined with the shear stresses and transformed to yield the zero surface normal and shear stresses present on the curved surface of the fillet. The tensile σ_{xx} stresses peak near the region where the fillet becomes tangent to the flange and are about 9 percent higher than the maximum compressive σ_{xx} stresses. Figure 17 indicates the presence of tensile stresses in the vertical direction that are distributed throughout the fillet region. However, rather than being reduced as they progress into the fillet, these stresses are somewhat larger than those in the web and extend into the region where the fillet becomes tangent to the flange. The presence of a sizable vertical compressive stress near the center of the fillet region is also of interest. Of course, if the direction of the bending loads is reversed, this compressive stress will become a tensile stress. The implications for a composite material are obvious even from this isotropic, homogeneous case. That is, since the vertical tensile stresses in the fillet and gap material take on values on the same order of magnitude as occur in the web laminate reinforced with fibers in the vertical direction, failure may be expected to occur in these regions that are unreinforced in the vertical direction due to the combination of vertical tensile stresses and other stresses. The normal stresses (σ_{zz}) perpendicular to the plane of the model are not shown since they are proportional to the inplane stresses for this homogeneous material in a state of generalized plane strain.

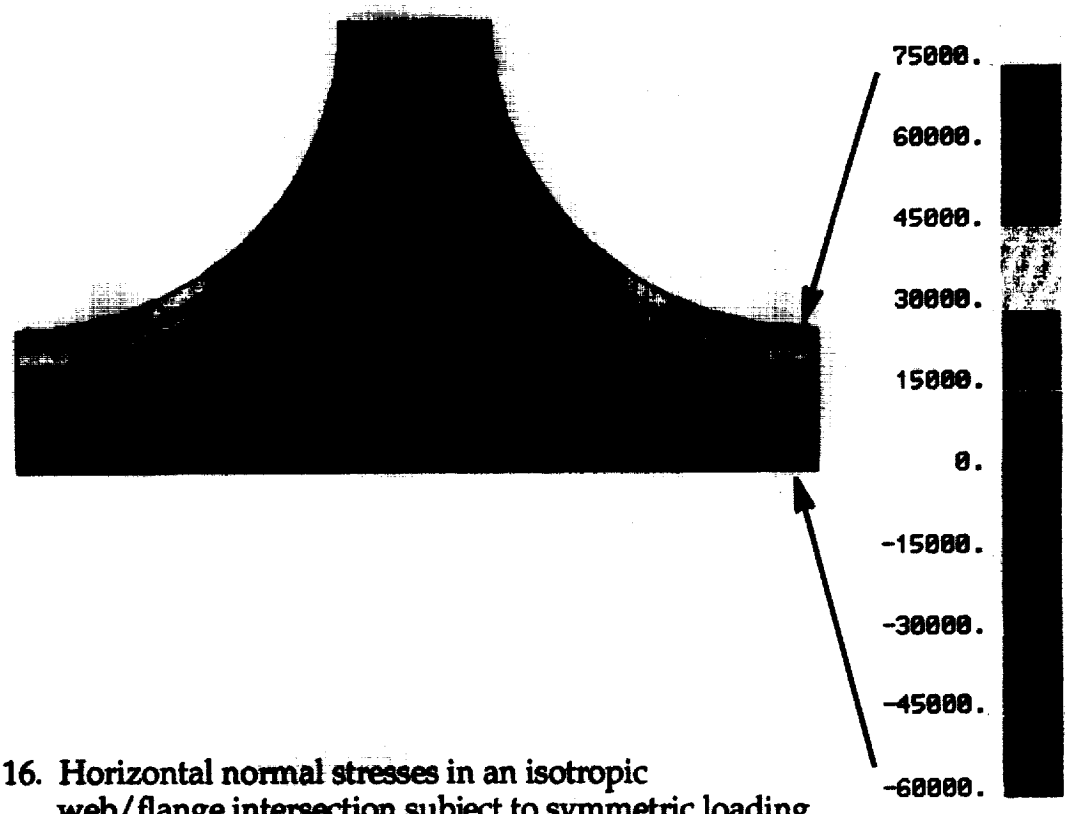

Figure 16. Horizontal normal stresses in an isotropic web/flange intersection subject to symmetric loading.

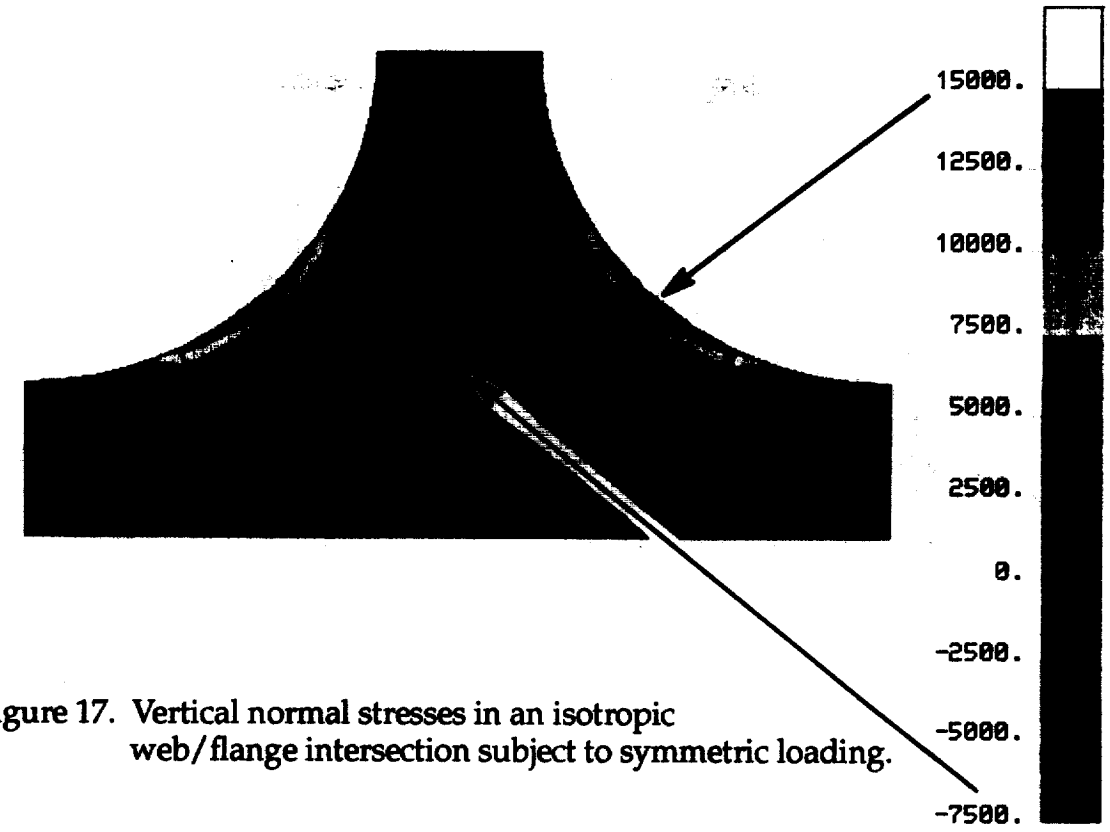

Figure 17. Vertical normal stresses in an isotropic web/flange intersection subject to symmetric loading.

Contour plots for the intersection region shear stresses (τ_{xy}) in the plane of the model are presented in Figure 18. The shear stresses show a tendency to peak near the fillet region. Again, the implication for composite materials subjected to a combination of inplane and transverse tensile stresses and transverse shear stresses is clear since this combined state of stress can lead to failure in the laminated materials.

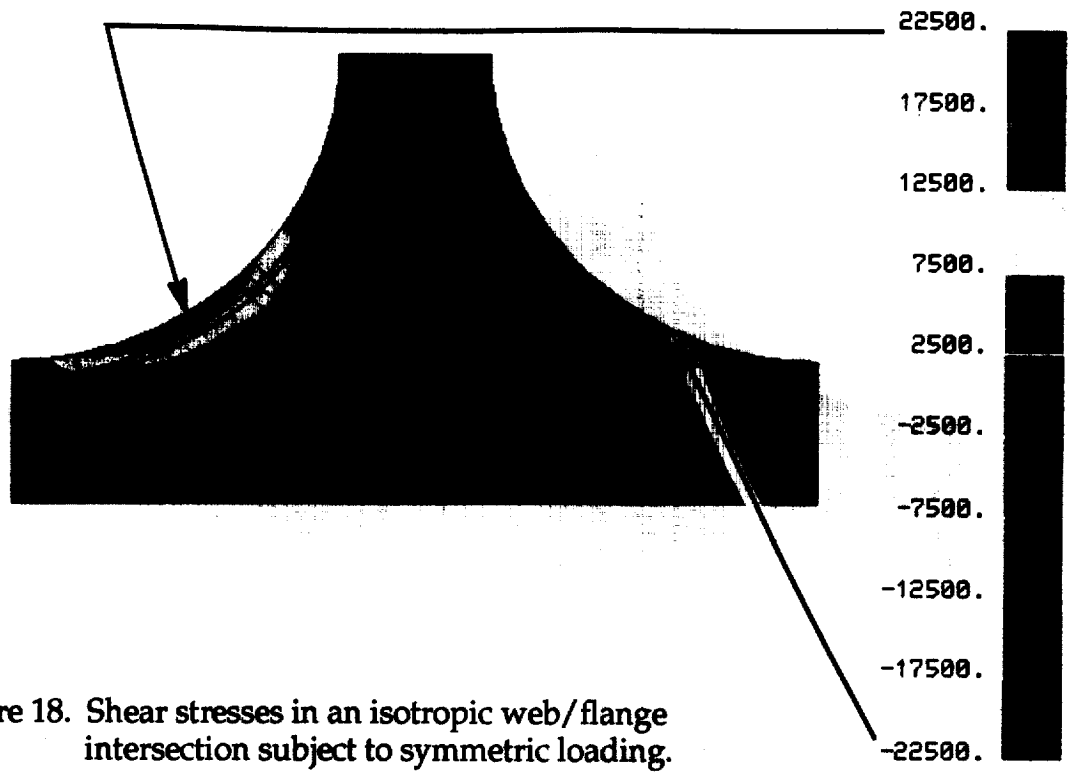

Figure 18. Shear stresses in an isotropic web/flange intersection subject to symmetric loading.

Similar results were obtained for a second model with a 1/2 inch fillet radius. A finer mesh was used in the fillet region in this case since considerably more material is now present in this region. The loads on the ends of the flanges were the same as in the first model, reducing the moment at the tangent point of the larger fillet by 33 percent. The maximum σ_{xx} (horizontal) and σ_{zz} (out-of-plane) stresses were predictably reduced by this same factor compared to the first model. The σ_{yy} (vertical) stresses and the τ_{xy} (shear) stresses were reduced by 50 and 45 percent, respectively, when compared to the smaller radius configuration. This shows the added stress reduction in the intersection region that is due to the smoother geometric transition from the flange to the web that exists with the larger fillet radius. It should be noted, however, that the deflection of the flange ends for the 1/2 inch fillet radius section model is approximately half that of the 1/4 inch fillet radius section. Therefore, if the end loads were actually generated from a given imposed deflection of the flange ends, as would be the case in an assembly of misaligned parts, the bending moment and therefore the stresses would actually be higher for the larger radius section than for its smaller radius counterpart which is considerably more flexible.

Antisymmetric Load Case

Results for this loading condition on the intersection region stresses in the model with a 1/4 inch fillet radius are shown in Figures 19 through 21 where these figures are the direct counterparts of the three figures discussed in the previous section. Most of the general trends regarding the type and distribution of stresses are the same for both types of loading conditions. However, while the results for the symmetric load case indicate that the critical location is near the fillet/flange intersection, the critical location changes to the fillet/web intersection region when the loading becomes antisymmetric about the web centerline. The other notable exceptions are that the shear stresses are only reduced by 23 percent and the vertical stresses in the web are unchanged in the antisymmetrically loaded 1/2 inch fillet radius section compared to the 1/4 inch configuration.

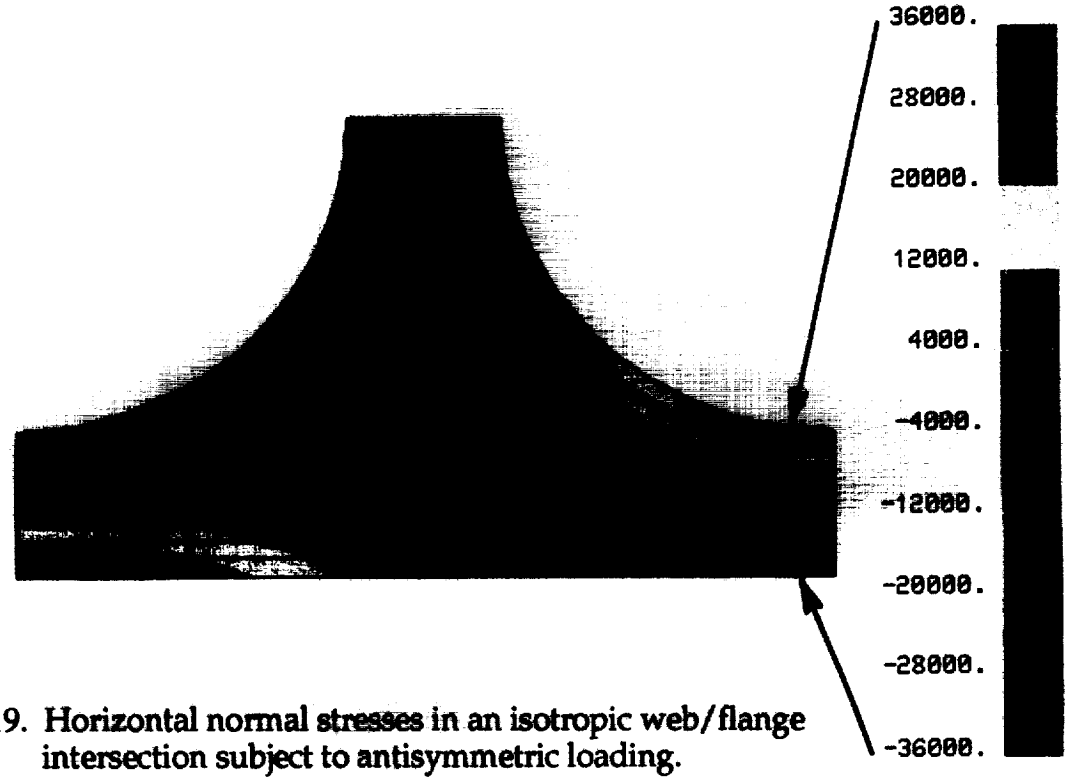

Figure 19. Horizontal normal stresses in an isotropic web/flange intersection subject to antisymmetric loading.

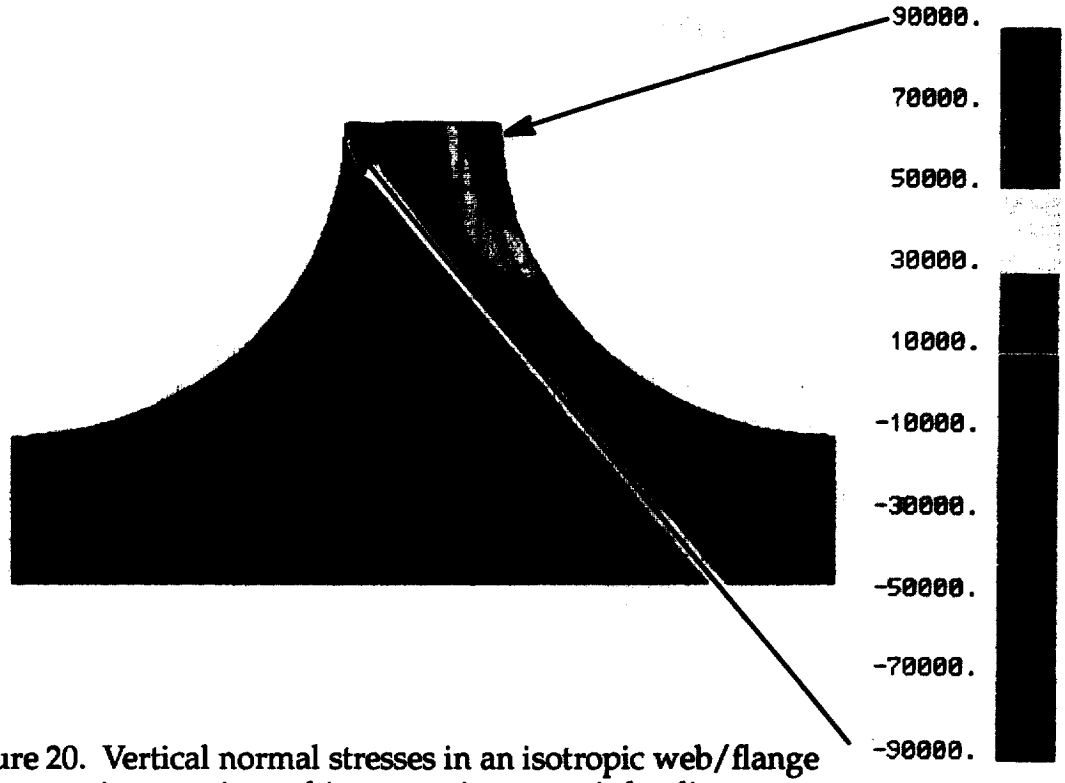

Figure 20. Vertical normal stresses in an isotropic web/flange intersection subject to antisymmetric loading.

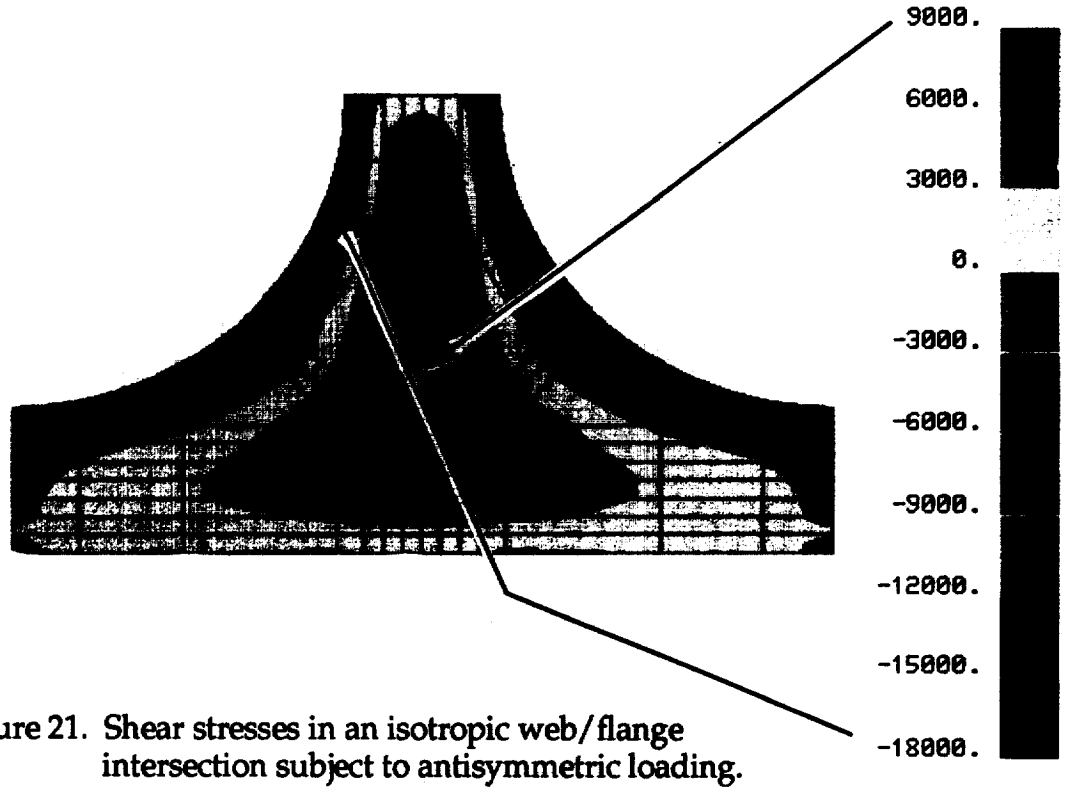

Figure 21. Shear stresses in an isotropic web/flange intersection subject to antisymmetric loading.

Models were also created for two T–shaped SiCf/Al sections representative of the specimens tested as discussed earlier. The level of detail, as shown by the 1/4 inch radius model in Figure 22, is greater than in the isotropic models. Here each ply was modeled by a separate second order element in the thickness direction. Three–dimensional anisotropic stiffness coefficients were computed for plies with 0, 90, +45, and –45 degree orientations. The following unidirectional lamina properties were used for this purpose:

$E_{11}/E_{22} = 4.5$	$E_{33}/E_{22} = 1.0$	$E_{22} = 41.37$ GPa. (6.0Msi.)
$G_{12}/E_{22} = 0.646$	$G_{23}/E_{22} = 0.397$	$G_{13}/E_{22} = 0.646$
$\nu_{12} = 0.26$	$\nu_{13} = 0.26$	$\nu_{23} = 0.26$

The web and flange stacking sequences are the same as used in the fabricated sections. The gap between the preconsolidated portion of the web and flange laminates is assumed to be filled with the same 0–degree material as used in the fillet and for the results to be presented the gap is assumed to be 0.02 inches in the vertical direction. The 0–degree fiber direction is perpendicular to the plane of the model.

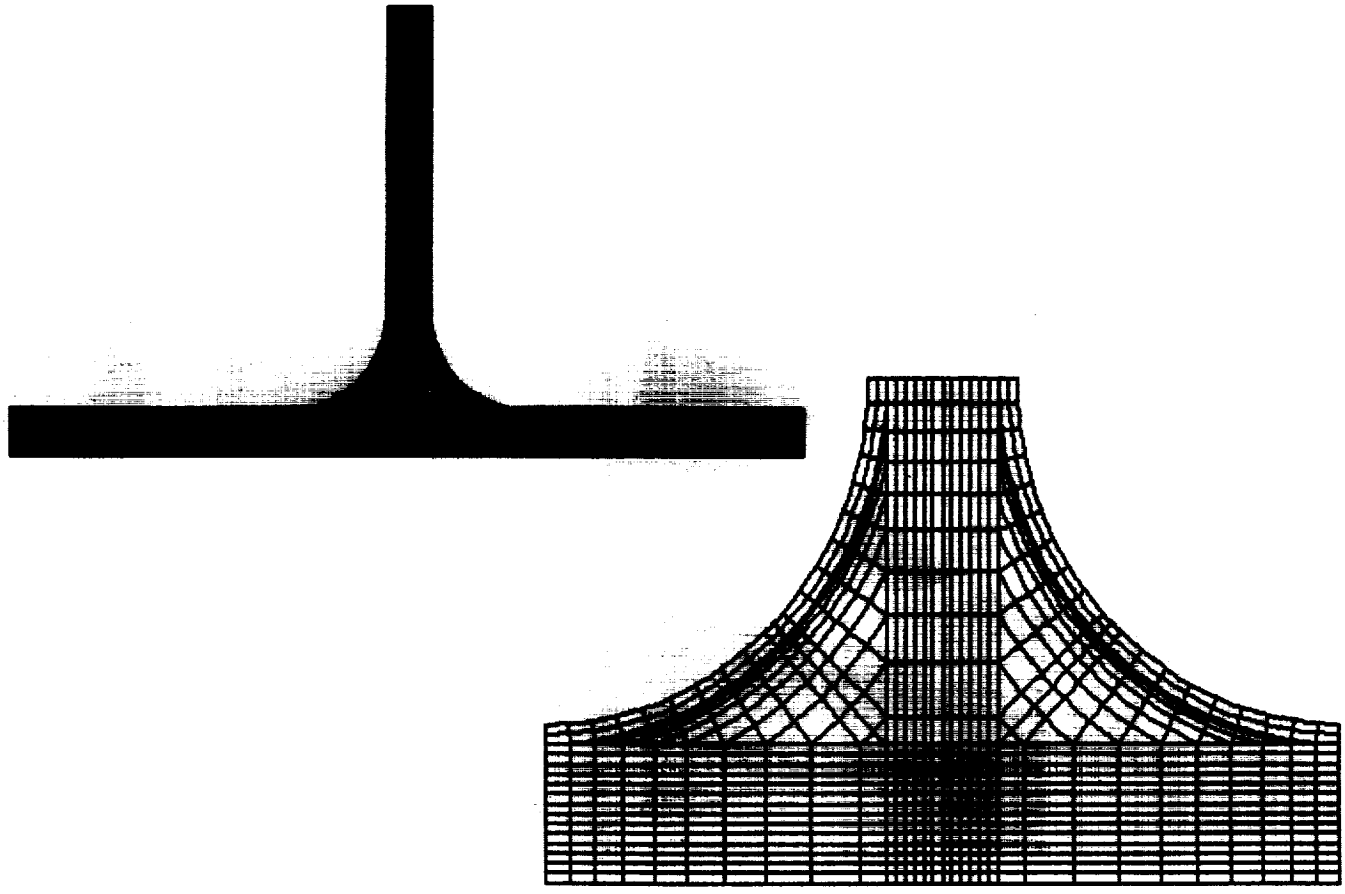

Figure 22. Finite element model mesh pattern for a typical MMC T–specimen with a 1/4 inch fillet radius and a close–up view of the intersection region.

Stresses were computed using a 1–2–3 coordinate system in which the 1–direction is along the width of the flange and the height of the web, and is circumferential in the "fillet wrap" plies and the fillet material. The 2–direction is in the ply–thickness direction for the flange, web and wrap plies and is in the radial direction for the fillet material. The 3–direction is normal to the plane of the cross–section. The material in the "gap" is assigned the same coordinate directions as the web. Therefore, the σ_{11} stresses are in the fiber direction for 90–degree plies and in the inplane transverse direction for the 0–degree plies. They are in the circumferential transverse direction for the fillet and in the vertical transverse direction for the gap material. The σ_{22} stresses are interlaminar for the web, flange, and wrap plies. They are in the radial transverse direction for the fillet material and in the horizontal transverse direction for the gap material. The τ_{12} stresses are interlaminar or transverse shear stresses in all parts of the model. The σ_{33} stresses are in the fiber direction for 0–degree plies and the material in the fillet and gap. They are in the inplane transverse direction for 90–degree plies. Fiber–direction stresses for the 45–degree plies are not reported but may be obtained by transformation of the 1–2–3 direction stresses.

Symmetric Load Case

The same load magnitudes and direction and support conditions used for the isotropic models were used in the MMC study. The maximum deflections of the loaded ends of the flanges are 0.0408 inch and 0.0221 inch for the small and large radius sections, respectively. These deflections are slightly greater than those obtained for the isotropic models since the flange bending stiffness is largely governed by the E_{22} value of the 0–degree plies that dominate the flange laminate.

Results for the 1/4 inch fillet radius configuration – Contour plots of the stresses in the full symmetrically loaded model are shown in Figures 23 (a) through 25 (a) for the 1/4 inch fillet radius configuration. Detail plots of the intersection region comprised by the fillet material and the portion of the wrap plies in this region are shown as part (b) of each figure. Recall that for these latter plots the 1–direction is circumferential and the 2–direction is radial. Some of the contour plots show small local perturbations in the stresses from element to element that are clearly a result the attempt of the contour algorithm to show detail when in reality the stresses should vary more smoothly. The primary utility of the contour plots is to show the stress gradients and locations of maximum values. A summary of the largest values of the stresses will be given later in this section.

Figure 23 (a) indicates that the largest laminar stresses occur as expected in the wrap plies where the fillet becomes tangent to the flange. It may also be noticed that the base of the web and the "gap" is in compression in the vertical direction. Most importantly, large circumferential normal stresses also occur in the fillet material adjacent to the wrap plies as can be seen in Figure 23 (b). After examination of all the stresses, it will be seen that this stress dominates the predicted failure.

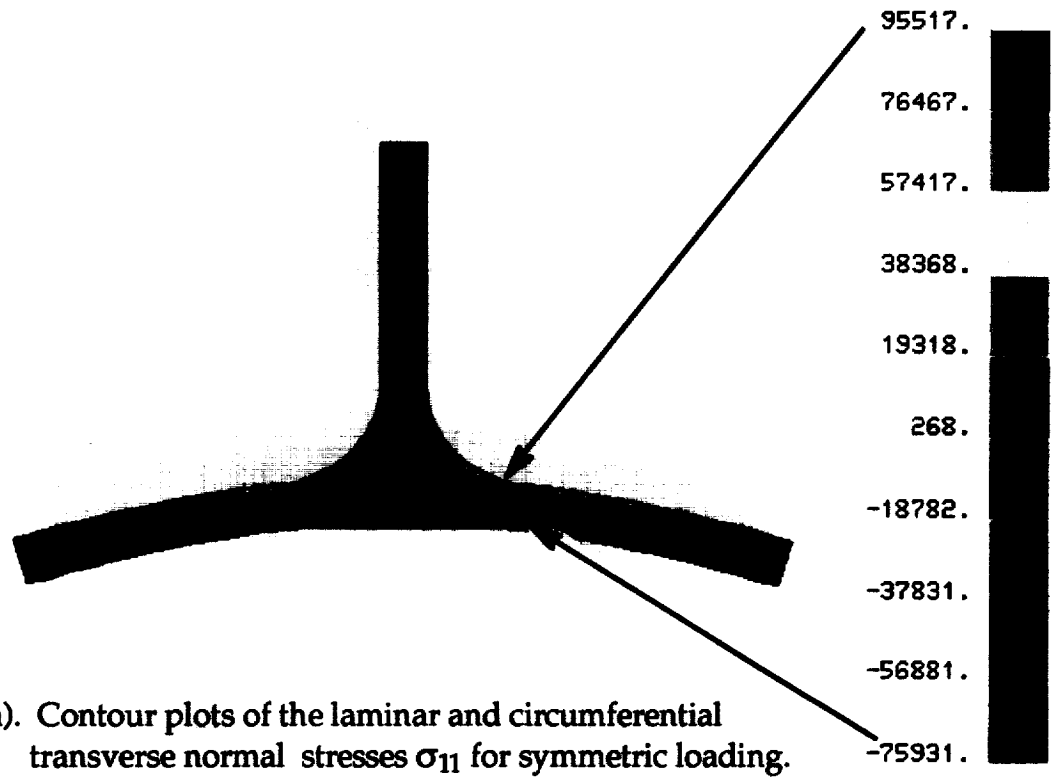

Figure 23 (a). Contour plots of the laminar and circumferential transverse normal stresses σ_{11} for symmetric loading.

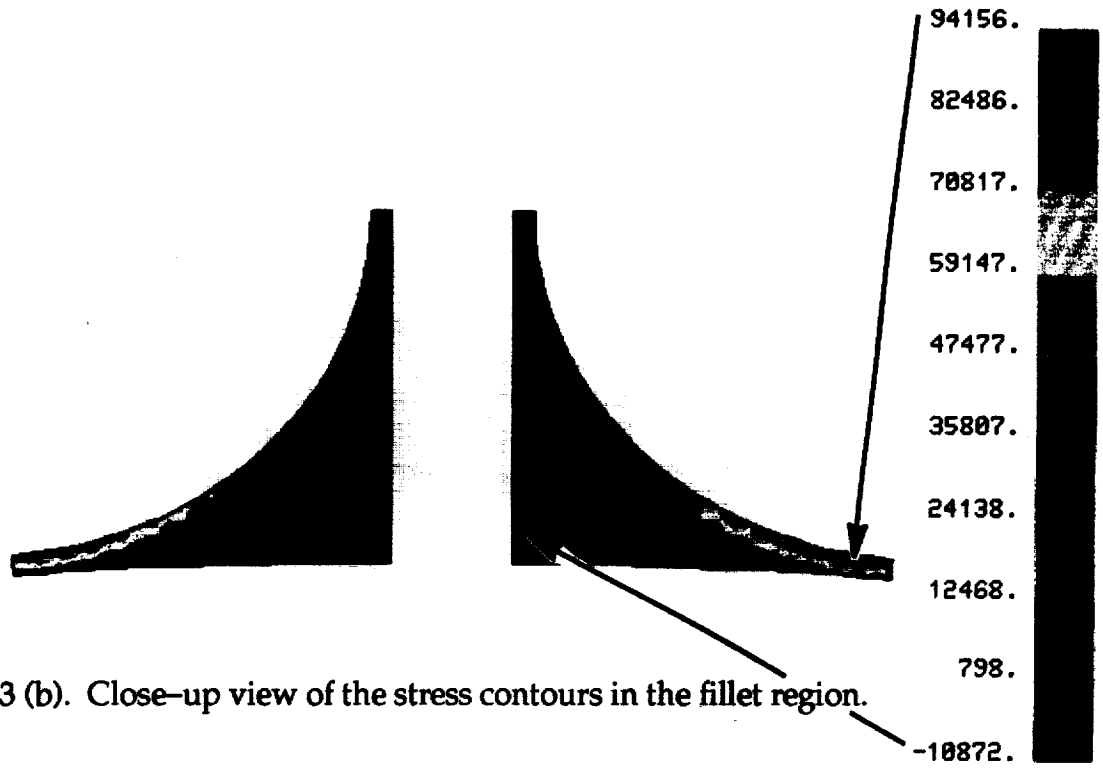

Figure 23 (b). Close-up view of the stress contours in the fillet region.

The interlaminar and radial normal stress contours are presented in Figure 24. As in the isotropic analyses, significant tensile stresses occur in the fillet and extend into the flange near the tangent point. Large tensile stresses also exit in the portion of the web that extends into the fillet. Large compressive stresses are present in the flange at the base of web near the "gap".

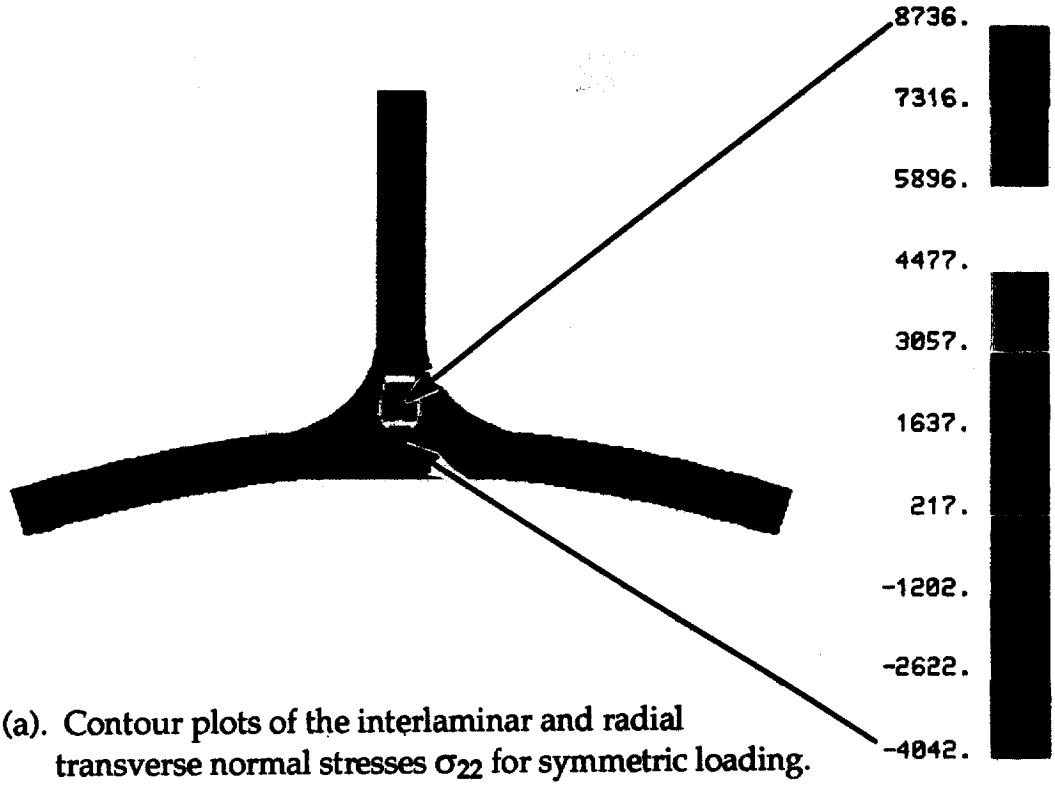

Figure 24 (a). Contour plots of the interlaminar and radial transverse normal stresses σ_{22} for symmetric loading.

The stress contours in the fillet region, shown in part (b), indicate that the radial tensile stresses are greatest where the fillet meets the web and are also large near the critical fillet–to–flange tangent point. The effect of the nonsymmetry of the part can be seen in the fillet region details of this symmetrically loaded model.

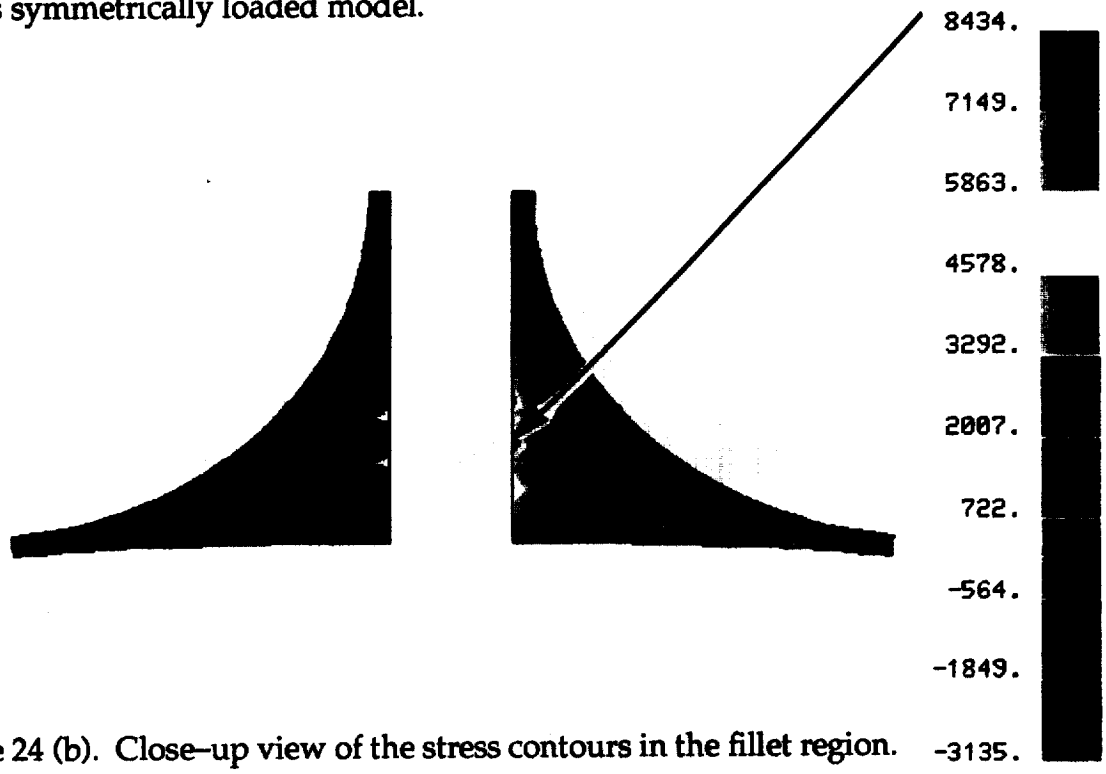

Figure 24 (b). Close–up view of the stress contours in the fillet region.

Figure 25 depicts the interlaminar and transverse shear stress distribution. Peak stresses occur in the center of the fillet and in the center of the flange directly under the fillet. Part (b) shows that sizable shear stresses extend throughout the fillet to the interface of the fillet with the wrap, web, and flange plies. However, unlike the normal stresses, the fillet/flange tangent point is not the location for the peak shear stresses.

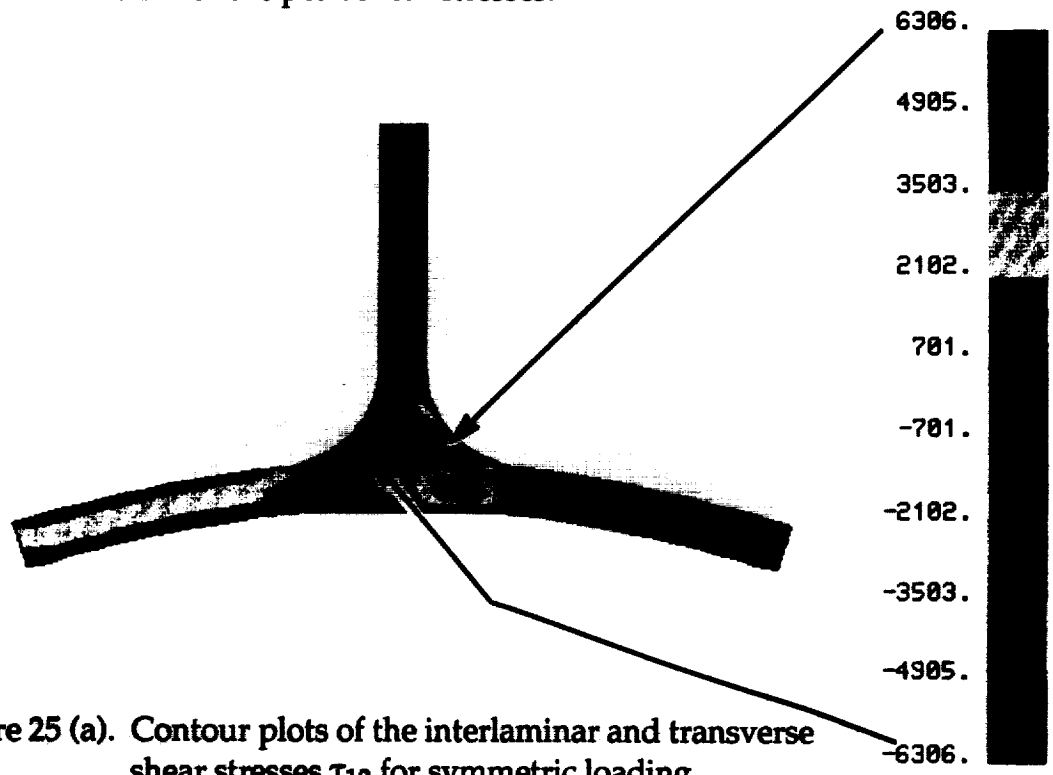

Figure 25 (a). Contour plots of the interlaminar and transverse shear stresses τ_{12} for symmetric loading.

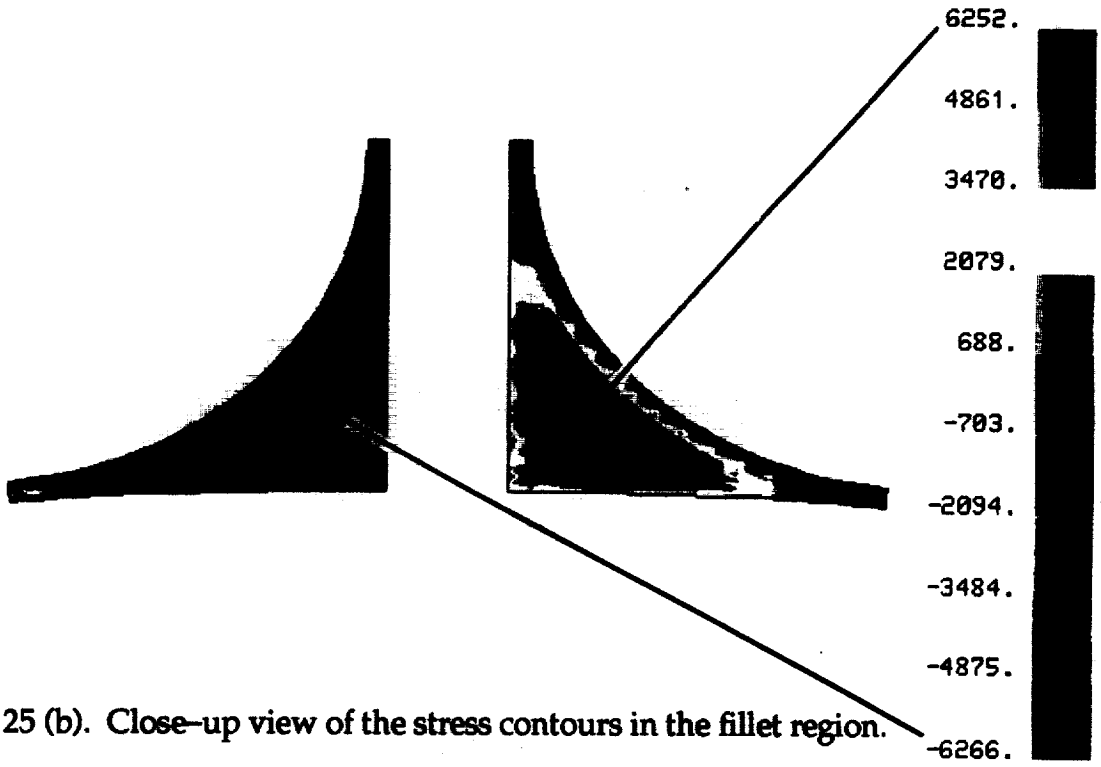

Figure 25 (b). Close-up view of the stress contours in the fillet region.

A summary of the largest positive and negative stresses σ_{11}, σ_{22}, and τ_{12} developed in various regions of the model is presented in the following figures. The abbreviations **Gp, Fil,** and **Wrp** stand for the gap, fillet, and fillet wrap material, respectively. **Flg.** and **Web** refer respectively to the complete flange and web laminates including the continuations of the "fillet wrap" plies. Again, the relative values of the stresses are of primary concern when evaluating these results.

The largest laminar and circumferential transverse normal stresses, shown in Figure 26, indicate that the stiff ±45–degree plies in the wrap and flange carry the bulk of the bending load. However the tensile stresses perpendicular to the 0–degree material in the fillet and the flange are also very high. Using a maximum stress failure criterion and ultimate stresses of 200 ksi in the fiber direction and 15 ksi transverse to the fiber direction, the fillet material would be the critical part of the specimen. If the sense of the bending were reversed, the tensile stresses in the 0–degree direction in the flange would become the critical stresses.

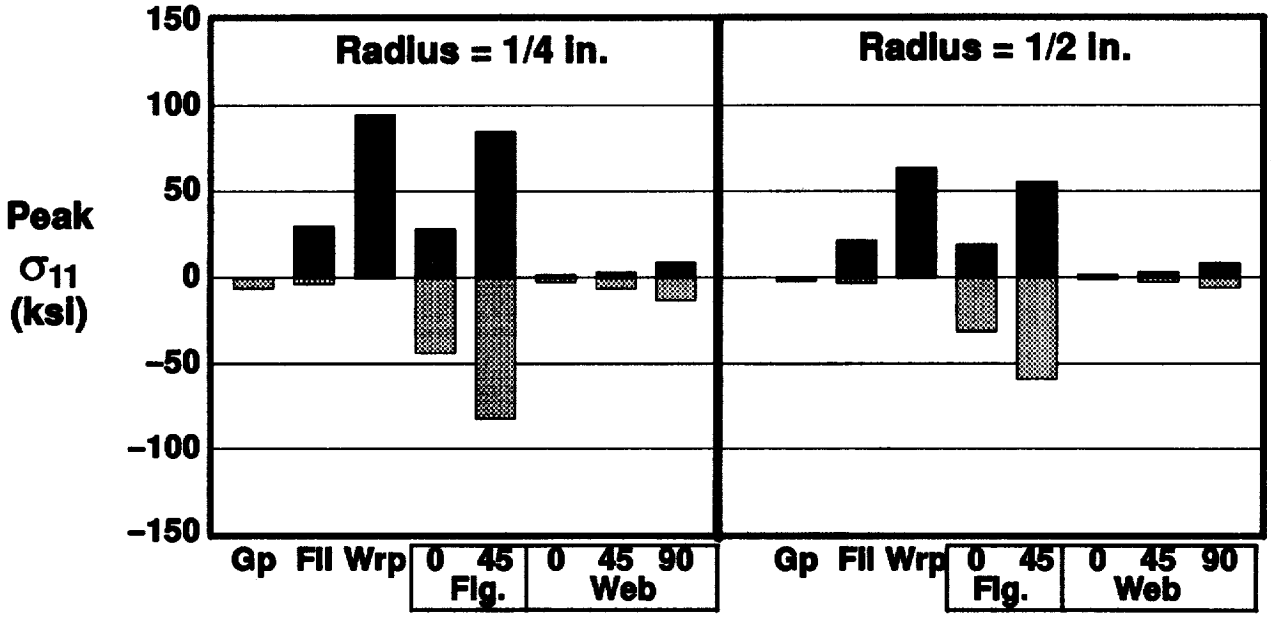

Figure 26. Peak laminar and circumferential transverse normal stresses for symmetric loading.

The largest interlaminar normal stresses are plotted in Figure 27. As seen from the contour plot, the portion of the web that extends into the fillet carries the highest interlaminar tensile stresses. However, these stresses are not nearly as severe compared to the 15 ksi ultimate transverse stress as are the circumferential transverse normal stresses in the fillet material (Figure 26) and would not govern part failure.

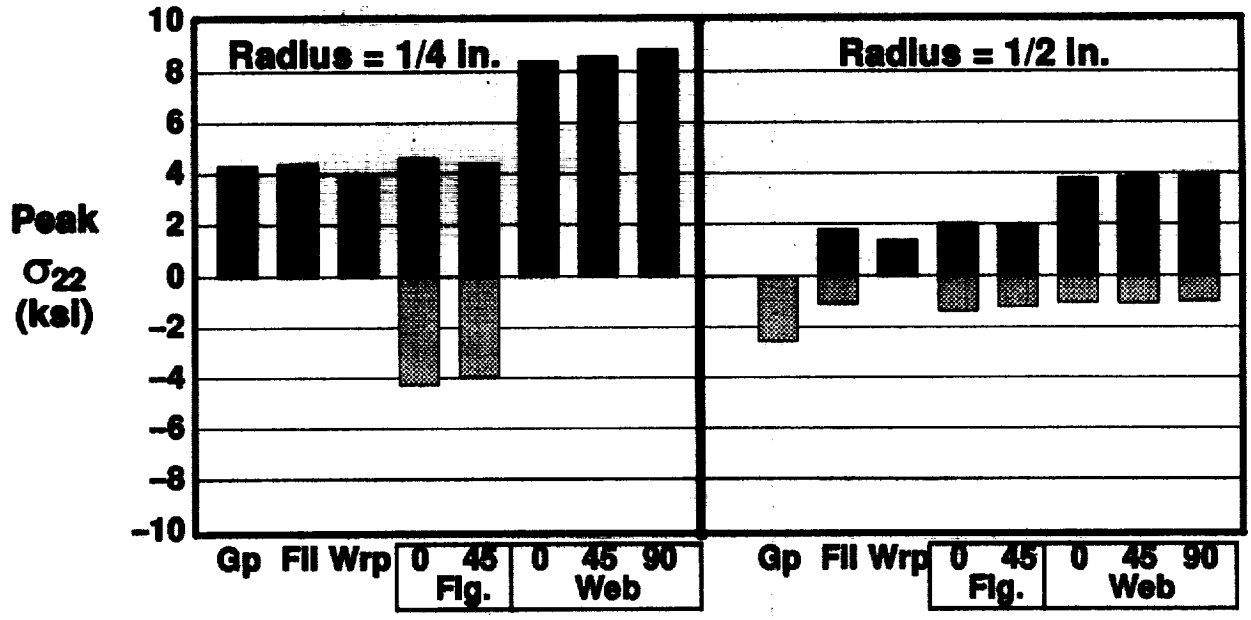

Figure 27. Peak interlaminar and radial normal stresses for symmetric loading.

The largest interlaminar and transverse shear stresses are shown in Figure 28. The largest shear stress occurs within the fillet material, but based on an ultimate stress of 15 ksi and a maximum stress criterion, it would not govern part failure.

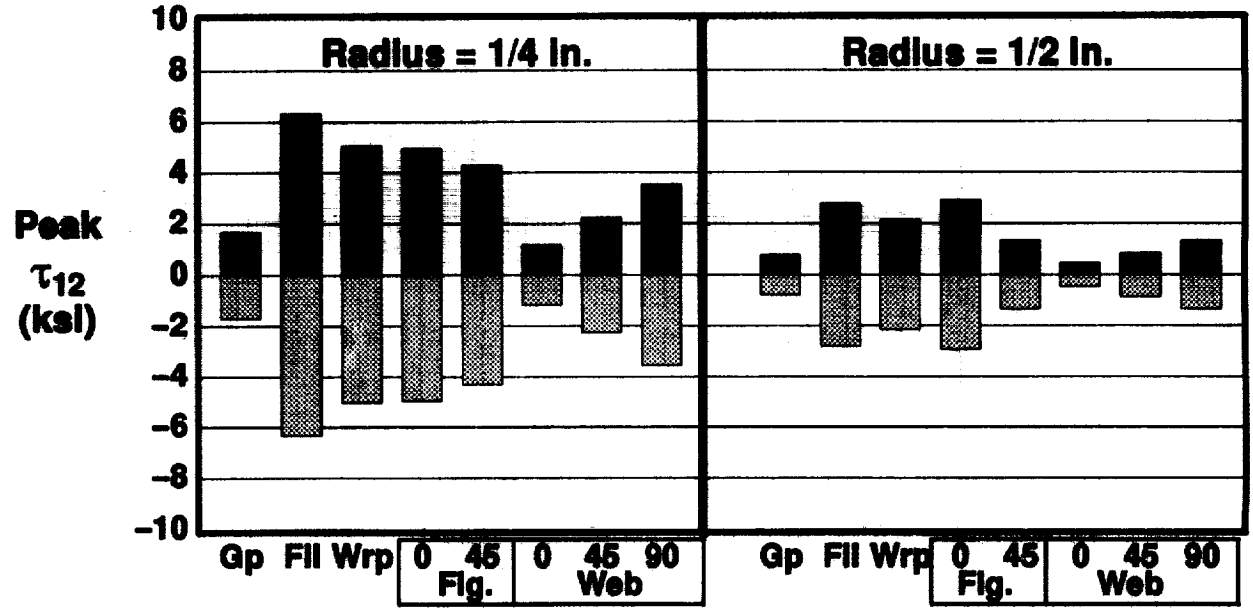

Figure 28. Peak interlaminar and transverse shear stresses for symmetric loading.

Since the total load applied to the model is 400 lbs/in, a maximum stress criterion predicts initial part failure at 200 lbs/in due to the transverse normal tensile stress in the fillet mate-

rial near the fillet/flange tangent point. A combined stress failure criterion, such as the one given in Reference 1, also predicts failure initiation near the same tangent point in the fillet material at almost the same load due to the dominance of the σ_{11} stress. The average test load for this configuration was 227 lbs/in. as shown in Figure 12. The corresponding average test load (Figure 13) for clamped edge specimens is 468 lbs/in., while the predicted load is 420 lbs/in.

Results for the 1/2 inch radius configuration – Contour plots of the stresses were also examined for the larger radius configuration. These plots are not included here since they are of the same character and since the locations of the peak stress points are unchanged from those found in the previous configuration. However, the magnitudes of these peak stresses are in most instances considerably lower than their counterparts in the smaller radius section.

A summary of stresses for the larger radius configuration is given in the second half of Figures 26–28. Comparison with their counterparts in the first half of these figures shows that the laminar stresses are reduced by approximately the same factor (33 percent) as is the applied moment (refer to the isotropic model discussion). The interlaminar normal stresses σ_{22} and the interlaminar shear stresses τ_{12}, however, are reduced by at least 41 percent, and generally by over 55 percent, for the flange, web, and wrap plies. The fillet material is exceptional in that the maximum circumferential transverse tensile stress is reduced by only 27 percent. This indicates that increasing the fillet radius is effective in reducing the interlaminar stresses in the layered material but is relatively ineffective in reducing the critical normal stresses in the fillet material. Since it is this stress and this part of the intersection region which dominates failure initiation, it would be necessary to explore other design variations, such as increasing the number of wrap plies or changing their fiber orientations in order to significantly and efficiently increase the load carrying capacity of the part. It may also be possible to improve the state of stress in the fillet by modifying the extent to which the web laminate extends into the fillet region. Changing the fillet material to one with a higher transverse strength to stiffness ratio could also be effective.

Antisymmetric Load Case

This loading condition was also chosen to be the same as used for the isotropic models, that is, 100 lbs/in vertical forces applied at the flange ends, antisymmetrically with respect to the web. The maximum horizontal deflections of the loaded ends of the flanges are 0.0668 inches and 0.0587 inches for the small and large radius sections, respectively. The maximum vertical deflections are 0.1219 inches and 0.0895 inches, respectively. These deflections are slightly lower than those obtained for the isotropic models since the web bending stiffness is largely governed by the stiff 90–degree plies near the outer surface of the web.

Results for the 1/4 inch fillet radius configuration – Contour plots of the stresses in the antisymmetrically loaded model are shown in Figures 29 through 31 for the 1/4 inch fillet radius configuration. Only the plots for the entire model are included since close–up views are not needed for clarification in these cases.

Figure 29 indicates the presence of large laminar tensile stresses in the web. The location of the 90–degree plies are clearly visible adjacent to the outermost plies (±45 degrees) in the web. Again large circumferential transverse normal stresses exist in the fillet material, however in this case the peak stresses occur near the fillet/web tangent point rather than near the fillet/flange tangent point.

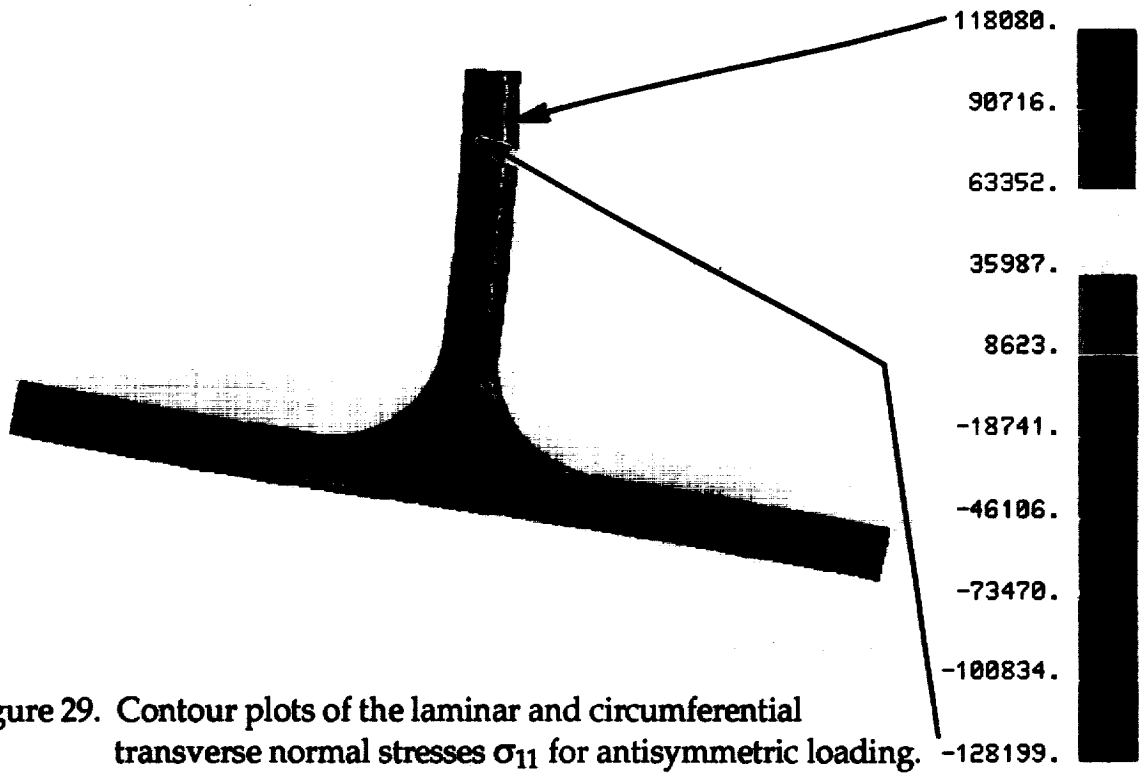

Figure 29. Contour plots of the laminar and circumferential transverse normal stresses σ_{11} for antisymmetric loading.

The interlaminar and radial transverse normal stress contours presented in Figure 30 show the largest values at the web/flange junction inside the fillet near the gap. Significant interlaminar stresses also exist near both fillet tangent points.

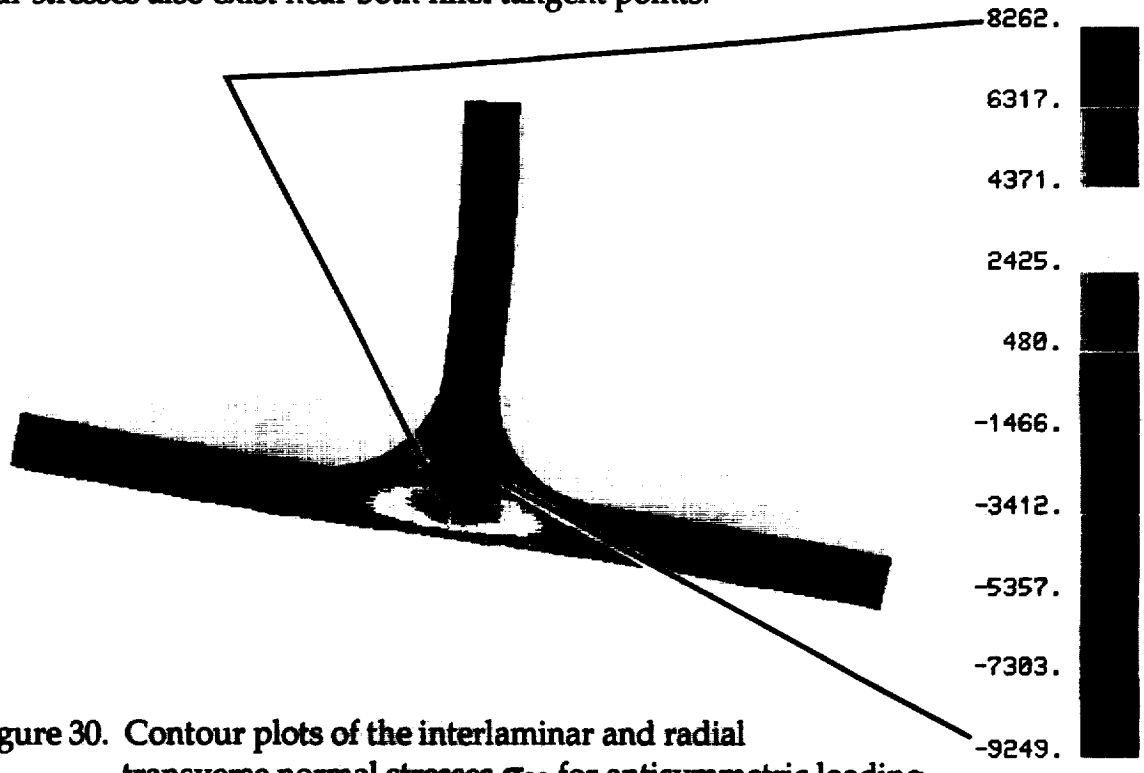

Figure 30. Contour plots of the interlaminar and radial transverse normal stresses σ_{22} for antisymmetric loading.

The largest interlaminar and transverse shear stresses occur in the portions of the web and flange inside the intersection region near the gap as shown in Figure 31. The gap material also experiences high shear stresses.

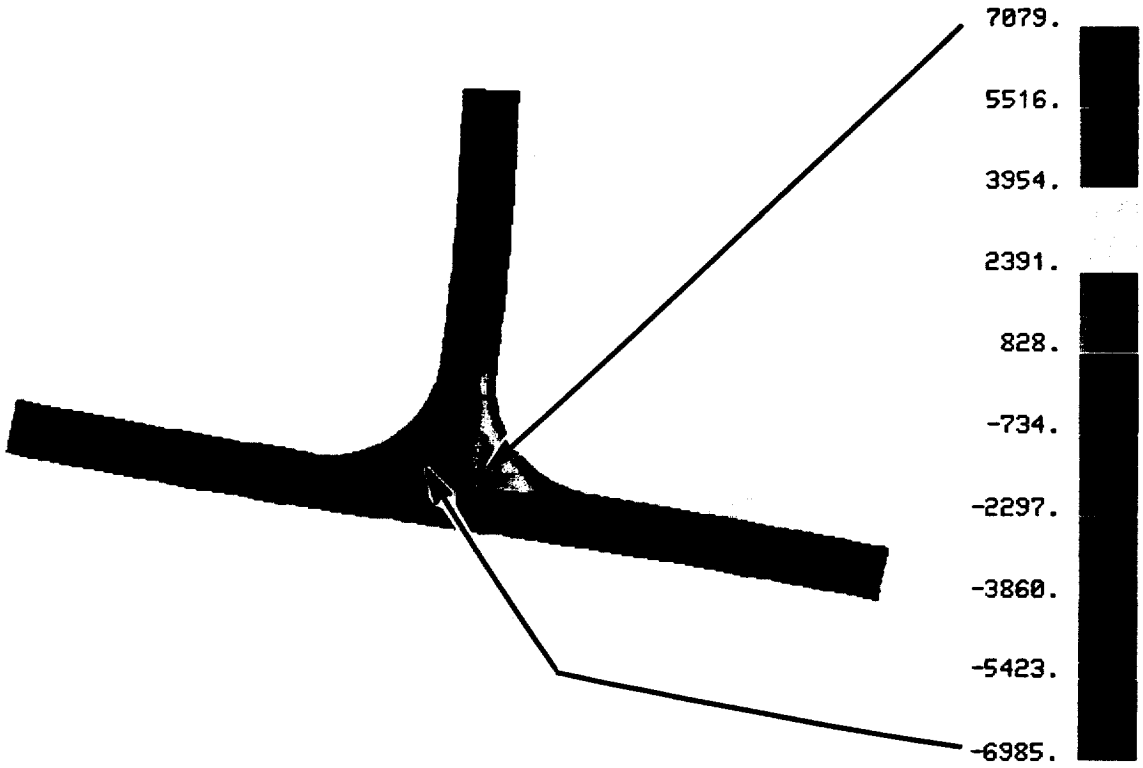

Figure 31. Contour plots of the interlaminar and transverse shear stresses τ_{12} for antisymmetric loading.

It can be seen from these figures that the conclusions drawn for the symmetric case generally apply for this case. The main exception is the location of the critical stresses. The antisymmetric loading forces this critical location to the region where the fillet becomes tangent to the web. The full-scale spar shown earlier in Figure 6 failed at this location indicating that a major anti-symmetric loading component was present. Since all actual loading conditions are a combination of symmetric and antisymmetric components, the fillet material near the tangent points to the web and/or flange is predicted to be the portion of the structure that will govern failure initiation.

A summary of the largest positive and negative stresses σ_{11}, σ_{22}, and τ_{12} developed in various regions of the model is presented in Figures 32–34. The peak circumferential normal stress in the fillet material is nearly identical to that in the symmetrically loaded case, the difference being in its location near the web/fillet tangent point. The normal stresses in the web are predictably higher than in the symmetrically loaded case.

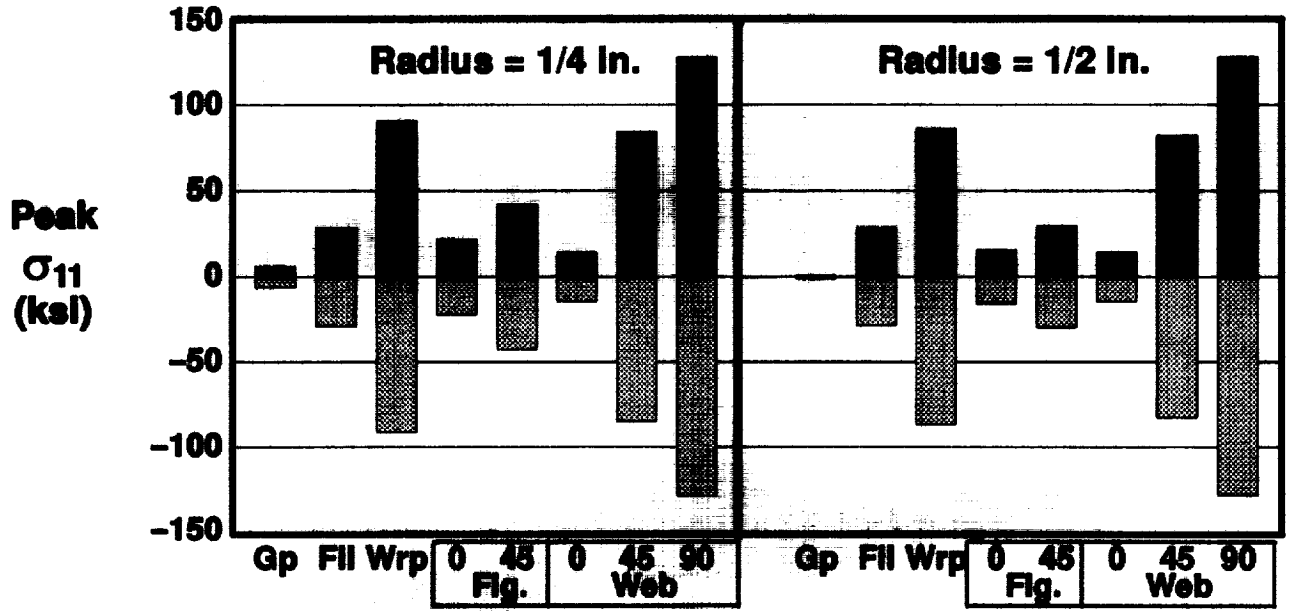

Figure 32. Peak laminar and circumferential transverse normal stresses for antisymmetric loading.

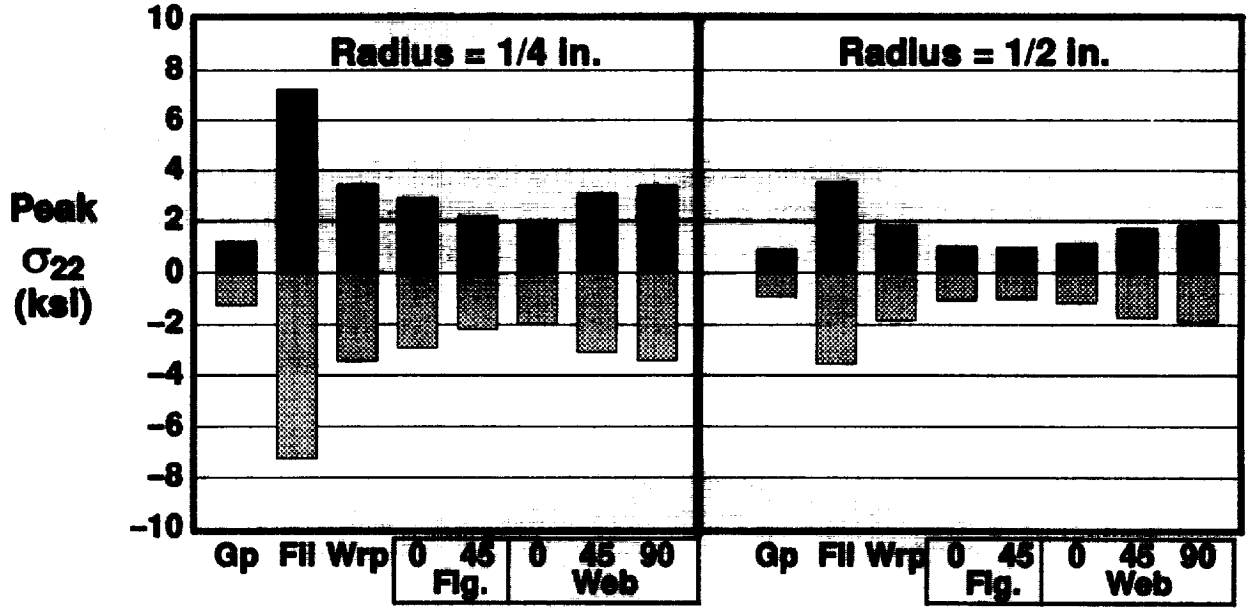

Figure 33. Peak interlaminar and radial normal stresses for antisymmetric loading.

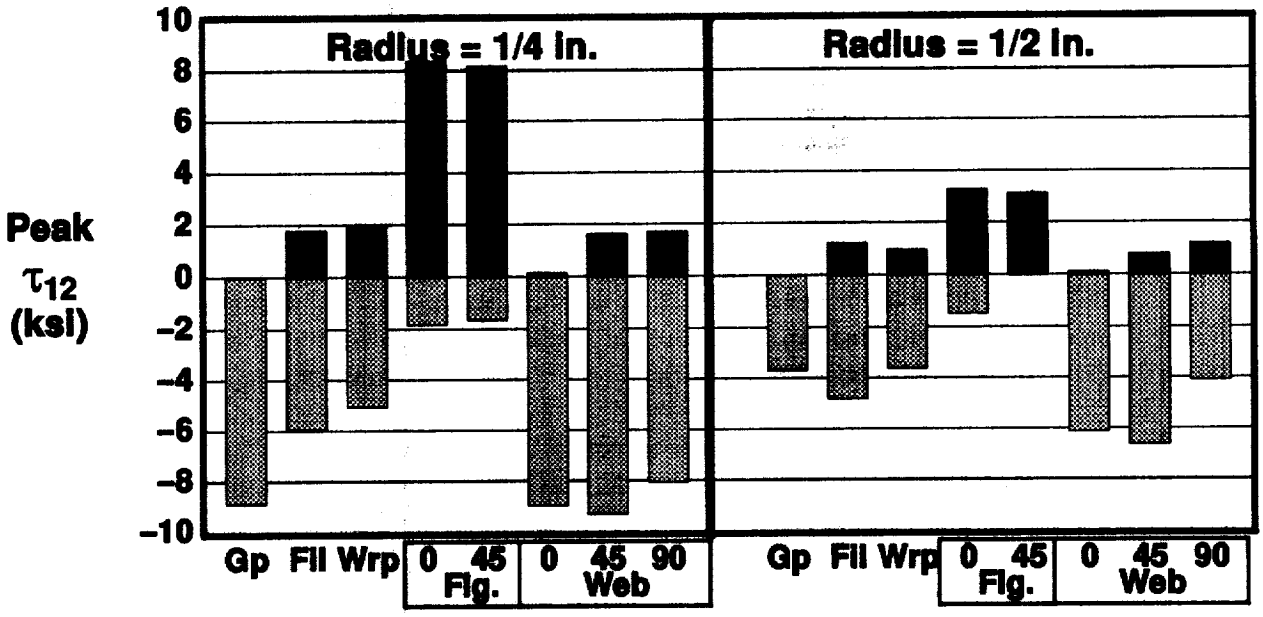

Figure 34. Peak interlaminar and radial shear stresses for antisymmetric loading.

Results for the 1/2 inch radius configuration – Contour plots of the stresses were also examined for the larger radius configuration. These plots are not shown here since they are of the same character and since the locations of the peak stress points are unchanged from those found in the smaller radius configuration. However, the effect of increasing the radius on the magnitudes of the stresses is different for the antisymmetric and symmetric loading cases.

A summary of magnitudes of the stresses for the larger fillet radius configuration is given in the second half of Figures 32–34. Comparison with their counterparts in the first half of the figure shows that the laminar stresses in the flange are reduced due to the reduced moment applied to the flange. However, the laminar stresses in the web are essentially unchanged when the fillet radius is increased. In addition, while the interlaminar normal stresses σ_{22} and the interlaminar shear stresses τ_{12} for the flange, web, and fillet wrap plies are reduced by 29 to 61 percent, the large circumferential transverse tensile stress in the fillet material is **unaffected** by the increase in fillet radius. Since this stress will dominate failure initiation, increasing the fillet radius is not effective at all in increasing the antisymmetric failure load. It is this fact that led to testing only symmetrically loaded T–specimens in the experimental program discussed earlier. Other design variations will need to be investigated if the antisymmetric load capacity is to be increased.

SUMMARY AND CONCLUSIONS

Tests on a full–scale, MMC (SiCf/Al), multi–spar box section representative of an advanced fighter vertical stabilizer revealed unexpected fatigue failures in the front and rear spars near the web/flange intersection. A separate full–scale static test on an identical multi–spar box failed just below design ultimate load with failure apparently initiating in the rear spar web/flange intersection region. An analytical and experimental investigation has been performed on an MMC T–section that is representative of this web/flange intersection and is subjected to local bending. Finite element modeling procedures have been developed which provide a rapid and

systematic way of generating detailed finite element models of various T–section configurations. The modeling and analysis approach has been applied to isotropic and MMC T–sections with 1/4 inch and 1/2 inch fillet radii. Tests have been performed on MMC specimens with several design variations in the intersection region. The analytical results obtained indicate that the peak stresses are generally lower for the larger fillet radius configuration than for the smaller fillet radius configuration, but that the degree of reduction depends on the character of the local bending.

Analysis results have been presented for loading cases that represent bending of the flange that is symmetric and anti–symmetric with respect to the web. In each case, significant interlaminar and transverse stresses occur in the fillet, in the portion of the web laminate that extends into the fillet, in the gap between the web and flange laminates, and in the flange where the fillet becomes tangent. For the symmetric loading, increasing the fillet radius is effective in reducing the interlaminar stresses in the web and flange but is not as effective in reducing the peak transverse normal stresses in the fillet material. For the anti–symmetric loading, increasing the fillet radius also reduces the interlaminar stresses in the web and flange but does not reduce the maximum transverse normal stresses in the fillet material that are the critical stresses for the material investigated. Additional simulations to investigate changes in the fiber orientations and number of wrap plies, fiber volume in the fillet material, the size of the "gap" between the web and flange laminates in the fillet region, alternate stacking sequences in the web and flange laminates, and alternate MMC systems are required to develop improved designs for the web/flange intersection.

Element tests have been conducted to experimentally evaluate eight intersection design variations. Failure was observed to initiate in the intersection region in all cases. Test failure loads within about 10 percent of the analytically predicted failure loads were obtained for the specimens that had good fabrication quality. Test failure loads much lower than predicted were obtained with specimens that had good laminate quality but poor consolidation in the filler material in the fillet and gap regions of the specimens. The critical need for reliable nondestructive quality evaluation (NDE) methods that can be applied to the fillet intersection regions of this class of commonly used structures is pointed out by these test results. In the absence of such NDE methods, designs for this region that are more defect tolerant are required.

REFERENCES

1. Brewer, J.C. and P. A. Lagace, "Quadratic Stress Criterion for Initiation of Delamination," Journal of Composite Materials, Vol. 22, No. 12, December 1988, pp. 1141–1155.

ACKNOWLEDGMENTS

The first two authors acknowledge support from LASC. This work was performed under the direction of the third author while he was employed by LASC, Georgia Division. All authors would like to thank Mr. Brian Cornell (LASC–GA) for his helpful review of the manuscript.